

Joint Estimation of Extreme Precipitation at Different Spatial Scales through Mixture Modelling

Jordan Richards^{A*}, Jonathan A. Tawn^B, and Simon Brown^C

^AComputer, Electrical and Mathematical Sciences and Engineering Division,
King Abdullah University of Science and Technology (KAUST)

^BSTOR-i Centre for Doctoral Training, Department of Mathematics and
Statistics, Lancaster University

^CHadley Centre for Climate Prediction and Research, Met Office, UK

*Correspondence to: jordan.richards@kaust.edu.sa

Abstract

Parsimonious and effective models for the extremes of precipitation aggregates that can capture their joint behaviour at different spatial resolutions must be built with knowledge of the underlying spatial process. Precipitation is driven by a mixture of processes acting at different scales and intensities. The specific process that drives the extremal behaviour of the aggregate will be dependent on the aggregate resolution; whilst high-intensity, spatially-localised convective events cause extreme high-resolution spatial aggregates, the contribution of low-intensity, large-scale fronts is likely to increase with the scale of the aggregate. Thus, to jointly model low- and high-resolution spatial aggregates, we require a model that can capture both convective and frontal events. We propose a novel spatial extreme values model which is a mixture of two components with different marginal and dependence models that are able to capture the extremal behaviour of convective and

frontal rainfall. Modelling extremes of the frontal component raises new challenges due to it exhibiting strong long-range extremal spatial dependence. Our modelling approach is applied to fine-scale, high-dimensional, gridded precipitation data, where we show that accounting for the mixture structure improves the joint inference on extremes of spatial aggregates over multiple regions of different sizes.

Keywords— extreme precipitation; spatial aggregates; spatial conditional extremes; mixture modelling

1 Introduction

River flooding is caused by prolonged heavy rainfall over a designated catchment area, with the size of such areas varying dramatically between rivers in the UK. For example, the approximate catchment areas of the UK river Lune, that flows through Lancaster, and the Severn, the largest river in the UK, are $1,300\text{km}^2$ and $11,000\text{km}^2$, respectively. Hence, a key aspect of river flood risk management is understanding the extremal behaviour of precipitation accumulations at different spatial scales. Whilst inference on precipitation extremes can be conducted at different spatial resolutions separately, and many studies have done so (see Institute of Hydrology (1999)), ideally we require an approach that can be used for joint estimation of these variables at multiple spatial scales simultaneously. The benefits of such an approach include a framework for modelling dependence between aggregates over different regions and physically consistent inference, i.e., a natural ordering for quantiles of aggregates over nested regions (Richards et al., 2021a). Moreover, this approach offers an increase in the reliability of inference on aggregates over lower-resolution spatial scales as more data will be used for modelling.

Building a parsimonious model for extreme precipitation at multiple spatial scales is difficult, as the important aspects of the underlying processes that drive the extremal behaviour of precipitation change with spatial resolution. Extreme precipitation is caused by a mixture of known and well-understood processes; convective storms are spatially localised events, over short time scales, and contribute to high intensity precipitation (Schroeder et al., 2018), whilst non-convective events, i.e., stratiform precipitation caused by frontal systems, are of much lower intensity but have a much larger area of effect and persistence (Berg et al., 2013, Catto and Pfahl, 2013, Gregersen et al., 2013). The distinction between the two types of events is an important consideration when modelling the upper-

tail behaviour of spatial aggregates, particularly as the size of the region over which we aggregate increases; the contribution of frontal events is likely to increase with the size of the region.

Richards et al. (2021a) develop methodology for joint inference on precipitation extremes at different spatial scales. Specifically, they perform inference on the upper-tail of the aggregate variable

$$\bar{R}_{\mathcal{A}} = \frac{1}{|\mathcal{A}|} \int_{\mathcal{A}} Y(s) ds, \quad (1)$$

where $\{Y(s) : s \in \mathcal{S}\}$ denotes a spatial process for some spatial domain $\mathcal{S} \subset \mathbb{R}^2$, and where $\mathcal{A} \subset \mathcal{S}$ is a sub-region of interest, with data available being realisations $Y_t = (Y_t(s_1), \dots, Y_t(s_d))$ for times $t \in \mathcal{T} = \{1, \dots, n\}$ and sampling locations $\mathbf{s} = (s_1, \dots, s_d) \subset \mathcal{S}$. To achieve this, they propose a model for the extremal behaviour of $\{Y(s) : s \in \mathcal{S}\}$ by adapting the spatial conditional extremes approach, first proposed by Wadsworth and Tawn (2019) and with extensions by Tawn et al. (2018), Shooter et al. (2019, 2021a,b), Huser and Wadsworth (2020), Simpson and Wadsworth (2021), Simpson et al. (2021). Realisations taken from this model are used to conduct inference on $\bar{R}_{\mathcal{A}}$ for numerous regions $\mathcal{A} \subset \mathcal{S}$ simultaneously. Whilst their approach improved on previous approaches by ensuring self-consistent inference across different \mathcal{A} and flexible extremal dependence modelling, they make the restrictive assumption that both the marginal and dependence behaviour $\{Y_t(s) : s \in \mathcal{S}\}$ is stationary with respect to time; we know that for precipitation this assumption is poor. Here we adapt the modelling approach of Richards et al. (2021a); we propose separate models for convective and non-convective precipitation and simulate events from both models to approximate the upper-tails of $\bar{R}_{\mathcal{A}}$ for \mathcal{A} corresponding to different scales. Further extensions of the approach of Richards et al. (2021a) include an approach for simulating non-convective events, which suffer particularly badly from boundary effects due to their long-range dependence; a discussion of these complications and our solutions is given in Section 3.

We begin by assuming that times t can be partitioned into two sets, denoted \mathcal{C} and \mathcal{N} , which correspond to “convective”, and “non-convective”, times respectively; that is, if $t \in \mathcal{C}$, then the observed field $\{Y_t(s) : s \in \mathcal{S}\}$ is a convective event, and similarly for non-convective events. This classification is performed using an algorithm developed at the Met Office Hadley Centre, UK (see Section 4.2). We assume that there exist two different processes $\{Y_{\mathcal{C},t}(s) : t \in \mathcal{C}\}$ and $\{Y_{\mathcal{N},t}(s) : t \in \mathcal{N}\}$, i.e., a convective, and non-convective, process respectively, and that these processes have different marginal

and dependence structure. For each process, both the marginal behaviour and dependence structures are stationary with respect to the corresponding time sets; that is, the process $\{Y_{\mathcal{C},k}(s)\}$ is identically distributed to $\{Y_{\mathcal{C},l}(s)\}$ for all $l, k \in \mathcal{C}$, and similarly for the non-convective process $Y_{\mathcal{N},t}$. We then define the mixture process $\{Y_{\mathcal{M},t}(s)\}$ by

$$\{Y_{\mathcal{M},t}(s) : s \in \mathcal{S}\} = \begin{cases} \{Y_{\mathcal{C},t}(s) : s \in \mathcal{S}\}, & \text{with probability } p_{\mathcal{C}}(t), \\ \{Y_{\mathcal{N},t}(s) : s \in \mathcal{S}\}, & \text{with probability } 1 - p_{\mathcal{C}}(t), \end{cases} \quad (2)$$

for $p_{\mathcal{C}}(t) \in [0, 1]$. As our interest lies in spatial, not temporal, aggregates, we thus drop the time index t and let $p_{\mathcal{C}} = |\mathcal{C}|/(|\mathcal{C}| + |\mathcal{N}|)$.

For $Y_{\mathcal{C}}$ and $Y_{\mathcal{N}}$ we adapt the approach proposed by Richards et al. (2021a), and in Section 2 propose slightly different parametric sub-models for the two processes, as we expect the mixture components to exhibit different extremal dependence structures. We quantify extremal dependence for a process $\{Y(s)\}$ using the upper tail index $\chi(s_A, s_B)$ (Joe, 1997) for all $s_A, s_B \in \mathcal{S}$, defined as

$$\chi(s_A, s_B) = \lim_{q \uparrow 1} \Pr\{Y(s_B) > F_{Y(s_B)}^{-1}(q) | Y(s_A) > F_{Y(s_A)}^{-1}(q)\}, \quad (3)$$

where $F_{Y(s_A)}$ denotes the distribution function of $Y(s_A)$. The measure $\chi(s_A, s_B)$ determines the extremal dependence class; if $\chi(s_A, s_B) > 0$ or $\chi(s_A, s_B) = 0$, then $Y(s_A)$ and $Y(s_B)$ are asymptotically dependent or asymptotically independent, respectively (Coles, 2001). Richards et al. (2021a) find evidence that the process $Y_{\mathcal{C}}$ exhibits asymptotic independence at all spatial distances, i.e., $\chi(s_A, s_B) = 0$ for all $s_A, s_B \in \mathcal{S}$, inferring that extreme events of $Y_{\mathcal{C}}$ occur increasingly more localised as the magnitude of the events gets larger. However, we find that $Y_{\mathcal{N}}$ exhibits asymptotic dependence at short-range and asymptotic independence at long-range.

Model inference is conducted by first estimating \mathcal{C} and \mathcal{N} for the observation times, which we do using the algorithm detailed in Section 4.2; we then fit separate models to the two classes of data using the inference framework described in Section 2.3.3. We simulate from our fitted models for $\{Y_{\mathcal{C}}(s)\}$ and $\{Y_{\mathcal{N}}(s)\}$ using a procedure described in Section 3, and then combine realisations from both models to estimate the upper-tail behaviour of $\bar{R}_{\mathcal{A}}$. To illustrate the improvements to modelling $\bar{R}_{\mathcal{A}}$ that our approach provides to the approach detailed by Richards et al. (2021a), we apply both approaches to

precipitation data from a convection-permitting climate model in Section 4. That is, we compare two modelling approaches for Y : an approach using the existing model, denoted throughout by $\{Y_{\mathcal{E}}(s)\}$, which ignores the mixture structure in Y ; and our improved approach where we use a mixture process with two components, i.e., $\{Y_{\mathcal{M}}(s)\}$, defined in (2). The two are equivalent when $p_{\mathcal{C}} = 0$ or $p_{\mathcal{C}} = 1$.

2 Modelling extremes of each mixture component

2.1 Overview

Following Richards et al. (2021a), we adopt a two-step modelling approach. We first standardise the data using the marginal model described in Section 2.2; this model is presented for a generic stationary process $\{Y(s) : s \in \mathcal{S}\}$, but is applicable separately for each of the processes $Y_{\mathcal{C}}, Y_{\mathcal{N}}$ and $Y_{\mathcal{E}}$. The marginal fits are used to perform site-wise standardisation of data to standard Laplace margins; we denote these standardised processes by $\{X_{\mathcal{C}}(s)\}$, $\{X_{\mathcal{N}}(s)\}$ and $\{X_{\mathcal{E}}(s)\}$.

To characterise extremal dependence, we use the spatial conditional extremes framework proposed by Wadsworth and Tawn (2019); this is detailed for a generic standardised process $\{X(s) : s \in \mathcal{S}\}$ in Section 2.3.1, but is applied, separately, to each of $\{X_{\mathcal{C}}(s)\}$, $\{X_{\mathcal{N}}(s)\}$ and $\{X_{\mathcal{E}}(s)\}$. Slight differences in modelling choices are made for the three processes, i.e., choices of parametric forms for some functions; discussion of these differences is provided in Section 2.3.2.

2.2 Marginal model

We model the site-wise marginals of $\{Y(s) : s \in \mathcal{S}\}$ using three components: GPD tails (Coles, 2001) above some high threshold $q_{\lambda}(s)$, the λ -quantile of $Y(s)$, the empirical distribution for the bulk and a discrete mass at the lower tail, denoted $p(s)$, which corresponds to the probability that no rain occurs at site $s \in \mathcal{S}$. The distribution function for $Y(s)$, for all $s \in \mathcal{S}$, is

$$F_{Y(s)}(y) = \begin{cases} p(s), & \text{if } y = 0, \\ \frac{1-\lambda-p(s)}{F_{Y_{+}(s)}(q_{\lambda}(s))} F_{Y_{+}(s)}(y) + p(s), & \text{if } 0 < y \leq q_{\lambda}(s), \\ 1 - \lambda \left[1 + \frac{\xi(y-q_{\lambda}(s))}{v(s)} \right]_{+}^{-1/\xi}, & \text{if } y > q_{\lambda}(s), \end{cases} \quad (4)$$

where $[x]_{+} = \max\{x, 0\}$, and where $\xi \in \mathbb{R}$, $v(s) > 0$ and $p(s) \geq 0$, $0 < \lambda < 1$ and $p(s) + \lambda < 1$; here $F_{Y_{+}(s)}(y)$ denotes the empirical distribution function of strictly positive values of $Y(s)$.

The marginal parameter functions $p(s)$, $q_\lambda(s)$ and $v(s)$ are represented through a basis of thin-plate splines. We estimate $p(s)$ using a logistic generalised additive model (GAM) (Wood, 2006) and estimate $q_\lambda(s)$ for all $s \in \mathcal{S}$ using additive quantile regression (Fasiolo et al., 2021); the latter technique is computationally expensive and so we use only a subset of sites for estimation. Richards et al. (2021a) propose a technique for estimating $q_\lambda(s)$ by fitting a thin-plate spline through point-wise estimates of $q_\lambda(s)$ for each $s \in (s_1, \dots, s_d)$; however, our approach provides more reliable estimates as more data are used for estimating the splines, rather than single quantile estimates. The scale parameter $v(s)$ is estimated by fitting a GPD GAM to the exceedances of $q_\lambda(s)$, i.e., $Y(s) - q_\lambda(s)$, with a fixed shape parameter ξ for all $s \in \mathcal{S}$ (Youngman, 2019). Our choice to fix ξ over space was fully supported by our data and is a common approach taken when modelling spatial characteristics of extreme rainfall as it reduces the risk of having parameter identifiability issues, see Thibaud et al. (2013), Zheng et al. (2015), Saunders et al. (2017) and Brown (2018).

Exploratory analysis of the data reveals that elevation is an important covariate in the marginal behaviour of precipitation; an observation supported by Coles and Tawn (1996), Cooley et al. (2007) and Cooley and Sain (2010). Hence, we allow $p(s)$, $q_\lambda(s)$ and $v(s)$ to vary with both location and elevation; separate spline bases are used for both. Each spline consists of as few knots as possible, i.e., four, to ensure that the splines are smooth; this is to make the marginal fits physically interpretable and to reduce over-fitting. Our approach for inference differs from that proposed by Richards et al. (2021a) as we allow the margins to change with elevation.

2.3 Dependence model

2.3.1 Generic model

We model extremal dependence in the standardised process $\{X(s) : s \in \mathcal{S}\}$, given that it is extreme for some $s \in \mathcal{S}$, by conditioning on the process being above some high threshold u at a specified site $s_O \in \mathcal{S}$ for each $s_O \in \mathcal{S}$. The process $\{X(s)\}$ is assumed to be stationary with dependence a function of distance, i.e., $h(s_A, s_B) = \|s_A - s_B\|$ for $s_A, s_B \in \mathcal{S}$, and some distance metric $\|\cdot\|$. Following Wadsworth and Tawn (2019), we assume that there exists normalising functions $\alpha : [0, \infty) \rightarrow [0, 1]$,

with $\alpha(0) = 1$, and $\beta : [0, \infty) \rightarrow [0, 1]$, such that for each $s_O \in \mathcal{S}$, as $u \rightarrow \infty$,

$$\left(\left\{ \frac{X(s) - \alpha\{h(s, s_O)\}X(s_O)}{\{X(s_O)\}^{\beta\{h(s, s_O)\}}} : s \in \mathcal{S} \right\}, X(s_O) - u \right) \Big| \left(X(s_O) > u \right) \xrightarrow{d} \left(\left\{ Z(s|s_O) : s \in \mathcal{S} \right\}, E \right), \quad (5)$$

where E is a standard exponential variable, the process $\{Z(s|s_O)\}$ is non-degenerate for all $s \in \mathcal{S}$ where $s \neq s_O$ and it is independent of E . That is, there is convergence in distribution of the normalised process to $\{Z(s|s_O) : s \in \mathcal{S}\}$, termed the residual process and $Z(s_O|s_O) = 0$ almost surely.

In terms of a parametric specification of α , we also follow Wadsworth and Tawn (2019) and let

$$\alpha(h) = \begin{cases} 1, & h \leq \Delta, \\ \exp(-\{(h - \Delta)/\kappa_{\alpha_1}\}^{\kappa_{\alpha_2}}), & h > \Delta, \end{cases} \quad (6)$$

where $\Delta \geq 0$ and $\kappa_{\alpha_1}, \kappa_{\alpha_2} > 0$. This function determines the strength and class of extremal dependence within $\{X(s)\}$, see (3); allowing asymptotic dependence up to distance Δ from s_O , and asymptotic independence thereafter, with strength of dependence decreasing with α . Setting $\Delta = \infty$ and $\beta(h) = 0$ for all $h \geq 0$ makes $X(s)$ an r -Pareto process, which have been used for aggregated precipitation modelling by de Fondeville and Davison (2020).

Richards et al. (2021a) impose that the residual process $Z(s|s_O)$ for $s \in \mathcal{S}$ has delta-Laplace margins with location, scale and shape parameters determined by the spatial functions $\mu : [0, \infty) \rightarrow \mathbb{R}$, $\sigma : [0, \infty) \rightarrow [0, \sqrt{2}]$ and $\delta : [0, \infty) \rightarrow [1, \infty)$, respectively. We denote this by $\text{DL}(\mu\{h(s, s_O)\}, \sigma\{h(s, s_O)\}, \delta\{h(s, s_O)\})$, where the delta-Laplace density is $\delta\{2k\sigma\Gamma(1/\delta)\}^{-1} \exp\{-|(z - \mu)/(k\sigma)|^\delta\}$ for $z \in \mathbb{R}$ and $\mu \in \mathbb{R}, \sigma > 0$ and $\delta > 0$, where Γ denotes the standard gamma function and $k^2 = \Gamma(1/\delta)/\Gamma(3/\delta)$. Dependence within $\{Z(s|s_O) : s \in \mathcal{S}\}$, for each $s_O \in \mathcal{S}$, is modelled using a standard form Gaussian process with a stationary Matérn correlation function, denoted ρ . We adopt the same parametric forms for β , μ , σ , δ and ρ as Richards et al. (2021a), unless stated otherwise in Section 2.3.2. These parametric forms allow the extremal dependence model for $\{X(s)\}$ to exhibit independence at long-range as $\alpha(h) \rightarrow 0$, $\beta(h) \rightarrow 0$, $\mu(h) \rightarrow 0$, $\sigma(h) \rightarrow \sqrt{2}$ and $\delta(h) \rightarrow 1$ when $h \rightarrow \infty$.

The function $h(s, s_O)$ accounts for potential anisotropy in the extremal dependence structure of $\{X(s)\}$. As Richards et al. (2021a), we define the distance metric $\|s_A - s_B\|$, which involves an

elliptical transformation of $(s_A, s_B) \in \mathcal{S} \times \mathcal{S}$ and then finds the great-circle, or spherical, distance between them; the metric is parametrised by $\theta \in [-\pi/2, 0]$ and $L > 0$ which control the rotation and coordinate stretching effect, respectively, with $L = 1$ corresponding to isotropy.

2.3.2 Differences for non-convective component

We apply the model described in Section 2.3.1 to each of X_C , X_N and X_E . For X_C and X_E , we use exactly the same parametric forms for the dependence functions as proposed by Richards et al. (2021a); for X_N , we adapt the β and σ functions, denoting these new forms β_N and σ_N .

Richards et al. (2021a) advocate the use of a β function for X_C , say β_C , that satisfies the property $\beta_C(0) = 1$. They illustrate that this, combined with small values of $\alpha(h) \approx 0$ for small h , allows the model X_C to exhibit short-range spatial roughness; a desirable property for a process generating convective precipitation events. As we expect X_N to generate much smoother spatial events, we do not require the property that $\beta_N(0) = 1$; to support this claim, we illustrate observations of Y_C and Y_N in Figure 2. We instead adopt the approach of Shooter et al. (2021b) and let

$$\beta_N(h) = \frac{\kappa_{\beta_1} h^{\kappa_{\beta_2}} \exp(-h/\kappa_{\beta_3})}{\max_{h_* > 0} \{h_*^{\kappa_{\beta_2}} \exp(-h_*/\kappa_{\beta_3})\}}, \quad (\kappa_{\beta_1} \in [0, 1], \kappa_{\beta_2} > 0, \kappa_{\beta_3} > 0), \quad (7)$$

so $0 \leq \beta_N(h) \leq 1$ for all $h \geq 0$ and $\beta_N(h) \rightarrow 0$ as $h \rightarrow \infty$ with $\beta_N(0) = 0$. In our application, we consider both forms of β for X_N , but found that (7) provided a better fitting model.

The scaling function σ_C gives long-range independence. However, non-convective events can have a very large spatial extent, e.g., up to $1000km$ (Houze Jr, 1997). Long-range independence is not required for X_N when the domain of interest \mathcal{S} is small enough, as in our application in Section 4. To ensure a better fitting model for X_N , we let the σ_N function be

$$\sigma_N(h) = \kappa_{\sigma_3} (1 - \exp\{-(h/\kappa_{\sigma_1})^{\kappa_{\sigma_2}}\}), \quad (\kappa_{\sigma_1} > 0, \kappa_{\sigma_2} > 0, \kappa_{\sigma_3} > 0), \quad (8)$$

which is equivalent to σ_C when $\kappa_{\sigma_3} = \sqrt{2}$.

2.3.3 Inference

Inference for each of the three extremal dependence models is conducted using the pseudo-likelihood procedure proposed by Richards et al. (2021a), which they illustrate works well for models

of this type and for application to precipitation data. This technique requires selection of a sub-sample of d_s triples of sampling locations, subject to the maximum pairwise distances subceeding a value of h_{max} km. Maximisation of a pseudo-likelihood is then conducted using observations of the process at these triples via a triple-wise censored likelihood. We require a censored likelihood to handle point masses in the marginals of $X(s)$ caused by zeroes in the marginals of $Y(s)$. The censoring threshold for $X(s)$, we denote $c(s)$, is found by transforming $p(s)$ to the Laplace scale, i.e., $c(s) = F_L^{-1}\{p(s)\}$, where F_L denotes the standard Laplace distribution. We apply this approach and use different values of h_{max} and d_s for each of the three processes; further details are provided in Section 4.4. Inference is conducted for model (5) by fixing a high threshold $u > 0$ and assuming that the limit holds in equality; the value of u differs between the three processes. Finding a threshold such that $Z(s|s_O)$ and E , defined in (5), are independent may be infeasible with mixtures of different dependence present in $X(s)$, e.g., for $X_{\mathcal{E}}(s)$. This provides further support for our use of separate extremal dependence models for the mixture components, as the assumptions made in (5) are more likely to hold when applied to $X_{\mathcal{N}}$ and $X_{\mathcal{C}}$, rather than $X_{\mathcal{E}}$, and at lower thresholds u ; we find the latter to be the case in our analysis.

3 Simulating events

3.1 Efficient simulation

To simulate from the fitted models for $\{Y_{\mathcal{C}}(s)\}$, $\{Y_{\mathcal{N}}(s)\}$ and $\{Y_{\mathcal{E}}(s)\}$, we need to extend the procedure proposed by Richards et al. (2021a) due to long-range dependence features of frontal rain; we present this technique for a generic $\{Y(s)\}$ and $\{X(s)\}$, but this approach can be applied to any of the three considered processes. The approach we propose is tailored to a specific aggregate region $\mathcal{A} \subset \mathcal{S}$, but our interest may lie in aggregates over multiple regions $\mathcal{A}_1, \dots, \mathcal{A}_m$ for $m \in \mathbb{N}$; to ensure that we can perform joint inference on aggregates at multiple scales, we let $\mathcal{A} = \cup_{i=1}^m \mathcal{A}_i$ throughout.

Richards et al. (2021a) discuss edge effects that occur when considering aggregates over regions $\mathcal{A} \subset \mathcal{S}$, as the simulation procedure never generates events for which the conditioning sites lies outside of the boundaries of \mathcal{S} but an extreme event is observed within \mathcal{A} . To address this issue, they proposed constraints for choosing \mathcal{A} ; they require that the boundaries of \mathcal{A} are at least $\tau > 0$ distance within the boundaries of \mathcal{S} . They choose the value of τ so that there was a predetermined small probability of observing a large event at any $s \in \mathcal{A}$ given that there is an extreme event at any single site outside of \mathcal{S} .

When $\{Y(s)\}$ exhibits particularly strong extremal spatial dependence, picking a suitable τ may not be feasible; in our application we find this to be the case for $\{Y_{\mathcal{N}}(s)\}$. To address this issue, we introduce a set of conditioning sites \mathcal{A}_c that satisfy $\mathcal{A}_c \supseteq \mathcal{A}$ and create realisations of $\{Y(s) : s \in \mathcal{S} : Y(s_O) > v \text{ for } s_O \in \mathcal{A}_c\}$. Whilst Richards et al. (2021a) set $\mathcal{A}_c = \mathcal{S}$, here, when it is possible to sample from locations outside of \mathcal{S} , we allow for cases where $\mathcal{A}_c \not\subseteq \mathcal{S}$, then using $s_O \in \mathcal{A}_c \setminus \mathcal{S}$ we observe a reduction in edge effects when s_O are sufficiently far from \mathcal{A} .

We now assume that \mathcal{S} is a set of dense discrete sites, i.e., the set of observed sampling locations $\mathcal{S} = \mathbf{s}$. When $|\mathcal{S}|$ is large, it may be computationally infeasible to simulate fields $\{Y(s) : \text{for all } s \in \mathcal{S}\}$, then instead we can simulate fields on a sufficiently dense sub-region $\mathcal{S}_s \subset \mathcal{S}$, where $\mathcal{A} \subset \mathcal{S}_s \subseteq \mathcal{A}_c$. Illustrations of \mathcal{A} , \mathcal{S} , \mathcal{S}_s and \mathcal{A}_c for our application are presented in Figure 1 and a heuristic for choosing both \mathcal{S}_s and \mathcal{A}_c is given in Section 3.2; these sets vary with the process considered.

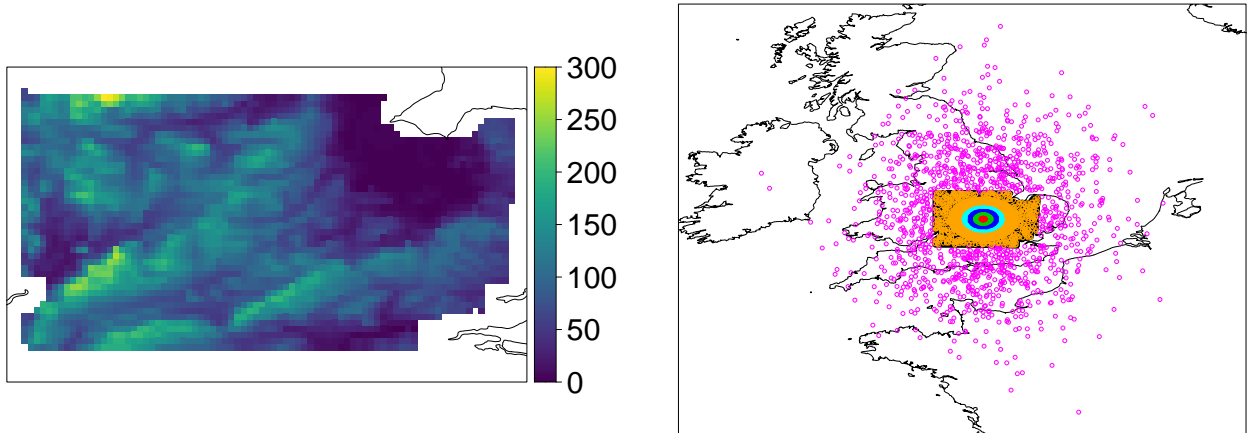


Figure 1: Left: A map of elevation (m) for the spatial domain \mathcal{S} of interest. Right: Regions \mathcal{A} , \mathcal{S}_s and \mathcal{A}_c . Aggregate regions \mathcal{A} with corresponding areas (179, 1263, 3257, 6200) – km^2 are coloured red, green, blue, cyan; regions include both the coloured and interior points and are numbered 1 to 4 in Figures S8 and 6. The orange and black points denote $\mathcal{S}_s \setminus \mathcal{A}$ and $\mathcal{S} \setminus \mathcal{S}_s$, respectively; the purple points outside of the boundaries of \mathcal{S} denote $\mathcal{A}_c \setminus \mathcal{S}_s$. Note that $n_s = 500$, $\tau = 27.5km$, and $n_c = 1250$; these values mean that $|\mathcal{S}_s| = 3625$ and $|\mathcal{A}_c| = 4875$.

To simulate $\{Y(s) : s \in \mathcal{S}_s\}$, we draw realisations of

$$\begin{aligned} & \left\{ Y(s) : s \in \mathcal{S}_s \right\} \left| \left(\max_{s \in \mathcal{S}} \{F_L^{-1}(F_{Y(s)}\{Y(s)\})\} > v \right), \right. \\ & \equiv \left\{ F_{Y(s)}^{-1}(F_L\{X(s)\}) : s \in \mathcal{S}_s \right\} \left| \left(\max_{s \in \mathcal{S}} \{X(s)\} > v \right), \right. \end{aligned} \quad (9)$$

for $v \geq u$, with probability

$$\Pr \left\{ \max_{s \in \mathcal{S}} \{F_L^{-1}(F_{Y(s)}\{Y(s)\})\} > v \right\}, \quad (10)$$

and otherwise draw realisations of

$$\left\{ Y(s) : s \in \mathcal{S}_s \right\} \left| \left(\max_{s \in \mathcal{S}} \{F_L^{-1}(F_{Y(s)}\{Y(s)\})\} < v \right), \right. \quad (11)$$

from the observed $\{Y(s) : s \in \mathcal{S}_s\}$. To draw $b \in \mathbb{N}$ realisations of (9), we use Algorithm 1.

Algorithm 1 Simulating conditional spatial fields corresponding to formulation (9)

1. For $i = 1, \dots, b'$ with $b' > b$:
 - (a) Draw a conditioning location $s_O^{(i)}$ from \mathcal{A}_c with uniform probability $1/|\mathcal{A}_c|$.
 - (b) Simulate $E^{(i)} \sim \text{Exp}(1)$ and set $x_i(s_O^{(i)}) = v + E^{(i)}$.
 - (c) Simulate a field $\{z_i(s|s_O^{(i)}) : s \in \mathcal{S}_s\}$ from the residual process model.
 - (d) Set $x_i(s) = x_i(s_O^{(i)})\alpha\{h(s, s_O^{(i)})\} + \{x_i(s_O^{(i)})\}^{\beta\{h(s, s_O^{(i)})\}} \times z_i(s|s_O^{(i)})$ for each $s \in \mathcal{S}_s$.
2. Assign each simulated field $\{x_i(s) : s \in \mathcal{S}_s\}$ an importance weight of

$$\begin{cases} \left\{ \sum_{s \in \mathcal{S}_s} \mathbb{1}\{x_i(s) > v\} \right\}^{-1}, & \text{if } \sum_{s \in \mathcal{S}_s} \mathbb{1}\{x_i(s) > v\} > 0, \\ 0, & \text{otherwise,} \end{cases} \quad (12)$$

for $i = 1, \dots, b'$, and sub-sample b realisations from the collection with probabilities proportional to these weights.

3. Transform each $\{x_i(s) : s \in \mathcal{S}_s\}$ to $\{Y_i(s) : s \in \mathcal{S}_s\}$ using the marginal transformation (4). If $x_i(s) \leq c(s)$, set $Y_i(s) = 0$, where for some $s' \in \mathcal{S}_s$, $Y_i(s')$ is above its $F_L(v)$ -th quantile.
-

Using Algorithm 1, we can draw realisations of $\{Y_C(s) : s \in \mathcal{S}_s\}$ and $\{Y_N(s) : s \in \mathcal{S}_s\}$; we can then use these to derive samples of $\{Y_M(s) : s \in \mathcal{S}_s\}$ by drawing from the samples of $\{Y_C(s) : s \in \mathcal{S}_s\}$ and $\{Y_N(s) : s \in \mathcal{S}_s\}$ with probabilities p_C and $1 - p_C$, respectively, see (2). Estimates of p_C and \bar{R}_A are both derived empirically; the former from the data and the latter from the simulated replicates. We denote estimates of \bar{R}_A derived using Y_M and Y_E by $\bar{R}_{M,A}$ and $\bar{R}_{E,A}$, respectively.

3.2 Choosing \mathcal{S}_s and \mathcal{A}_c

Although we have taken \mathcal{S} to be a discrete set, the heuristic we describe for choosing \mathcal{S}_s and \mathcal{A}_c can be extended to a spatially continuous setting. We begin by considering \mathcal{S}_s with $\mathcal{A} \subset \mathcal{S}_s \subseteq \mathcal{S}$ and then build \mathcal{A}_c dependent on \mathcal{S}_s . For Algorithm 1 Step 2, we require the approximation

$$\sum_{s \in \mathcal{S}_s} \mathbb{1}\{x_i(s) > v\} \approx \sum_{s \in \mathcal{S}} \mathbb{1}\{x_i(s) > v\}, \quad (13)$$

to account for the conditioning event in (9); we can improve the accuracy of this approximation by ensuring that sites in \mathcal{S}_s are sufficiently spread out across \mathcal{S} . We first set $\mathcal{S}_s = \{s \in \mathcal{S} : \min_{s_A \in \mathcal{A}} \{\|s - s_A\|\} \leq \tau\}$ as we expect extreme events within this set to have the largest effect on the tail behaviour of \bar{R}_A . If this choice of \mathcal{S}_s does not give a good approximation (13), then we additionally sample n_s sites uniformly at random across $\mathcal{S} \setminus \mathcal{S}_s$ and add these to \mathcal{S}_s .

In our application, we found that setting $\mathcal{A}_c = \mathcal{S}_s$ was a reasonable choice to make for Y_C and Y_E , as no improvement in our inference for \bar{R}_A was achieved by using $\mathcal{A}_c \supset \mathcal{S}_s$. However, this was not true for Y_N , which exhibits strong extremal dependence at even the greatest distances within \mathcal{S} . For such processes, we need to increase $\max_{s \in \mathcal{S}_s, s_O \in \mathcal{A}_c} \{\|s - s_O\|\}$ to ensure that we have conditioning sites s_O that are sufficiently far from \mathcal{A} such that simulated $\{Y(s)\} | (Y(s_O) > v)$ do not contribute to the extremes of \bar{R}_A . We take $\mathcal{A}_c \cap \mathcal{S} = \mathcal{S}_s$ and let $\mathcal{A}_c \setminus \mathcal{S} = \mathcal{S}^+$, with \mathcal{S}^+ a set of “fake” sampling locations without any observations and $|\mathcal{S}^+| = n_c$. We create \mathcal{S}^+ via a brute-force approach; we add independent Gaussian noise to the coordinates of a site in \mathcal{S} , rejecting new points $s^+ \in \mathcal{S}$.

In both cases, \mathcal{S}_s and \mathcal{A}_c should be chosen as large as is computationally feasible. Suitable values for the constants n_s, τ and n_c , and the variance of the noise term used to create \mathcal{A}_c , can be chosen through validation techniques, such as the simulated aggregate diagnostics (see Figures S8 and 6). If such fits look poor, one can increase the value of these constants to improve the fits.

4 Application

4.1 Data

Similar to that of Richards et al. (2021a), we consider average hourly precipitation rates (*mm*/hour) taken from the convection-permitting climate model UKCP18 (Lowe et al., 2018), 1980-2000. However,

the data here are on the finer resolution native climate model grid over a much larger domain \mathcal{S} and the dimension d is increased from 934 to 7526. We analysed the first and fourth ensemble members from the UKCP18; however, we present the latter analysis only, as we identified abnormally large and physically unrealistic values in the former. Each observation corresponds to the average over the assigned spatio-temporal grid-box. The sampling locations are $(2.2km)^2$ grid boxes and the spatial domain \mathcal{S} of interest is the region of the UK, approximately centred at Northampton and covering an area of $198 \times 231km^2$, pictured in Figure 1, with data only sampled over land. As extreme hourly precipitation is more likely to occur in summer, we use June-August observations only, 43200 fields, to avoid having to handle seasonality effects. We follow Richards et al. (2021a) and treat the centre of each grid box as a sampling location, and use the great-circle distance as our distance metric; we also set all values of the data less than $1 \times 10^{-5}mm/hour$ to zero¹.

4.2 Mixture component classification

To classify observation times as convective or not for the observed fields $\{y_t(s) : s \in \mathcal{S}, t = 1, \dots, n\}$, we use Algorithm 2 developed at the Met Office Hadley Centre, UK (Kendon et al., 2012, Roberts and Kendon, 2020) for summer precipitation data with gridded sampling locations. The algorithm classifies the observed field at time t as convective by using the gradient of the surface of $y_t(s)$ in a neighborhood around s_i for all $s_i \in \mathcal{S}$. This approach is a good classifier for convective rainfall as these events are highly localised, so large gradients are expected if convection is present. Gradients are calculated as the difference between precipitation rates at adjacent grid-boxes in a $n_g \times n_g$ grid, denoted \mathcal{L}_i , centered at s_i . If it is not possible to create \mathcal{L}_i , e.g., at the edges of \mathcal{S} , then s_i is removed. Any field not identified as convective is automatically classified as non-convective; this includes any fields with no rain at any $s \in \mathcal{S}$. Algorithm 2 involves four hyper-parameters: $g_l > 0, g_u > g_l, p^* \in [0, 1]$ and $n_g \in \{2d^* - 1, d^* \in \mathbb{N}\}$, we take to be $g_l = 0.01, g_u = 1$ and $p^* = 0.2$ and $n_g = 9$; these were tuned by the Met Office specifically for the climate model we use.

Algorithm 2 gives $|\mathcal{C}| = 13510$ and $|\mathcal{N}| = 29690$, so $\hat{p}_{\mathcal{C}} \approx 31.3\%$, with examples of classified fields of $\{Y_{\mathcal{C}}(s) : s \in \mathcal{S}\}$ and $\{Y_{\mathcal{N}}(s) : s \in \mathcal{S}\}$ presented in Figure 2. These selected fields were randomly sampled from fields which gave componentwise maxima for their respective processes. Fields identified as being non-convective appear smoother over space and with much lower marginal magnitude than

¹This level of precipitation would be recorded as zero by a rain gauge.

Algorithm 2 Identify convective fields

For all $t = 1, \dots, n$:

1. For all $i = 1, \dots, d$:
 - (a) Identify the $n_g \times n_g$ local neighbourhood \mathcal{L}_i for s_i , defined in Section 4.2.
 - (b) Evaluate all differences $\mathcal{G}_i = \{y_t(s_j) - y_t(s_k) : s_j, s_k \in \mathcal{L}_i\}$.
 - (c) Calculate the proportion $p_{g,i} = |\{g \in \mathcal{G}_i : g \geq g_u\}| / |\{g \in \mathcal{G}_i : g \geq g_l\}|$.
 - (d) If $p_{g,i} \geq p^*$, then $y_t(s_i)$ is labelled as convective and hence $t \in \mathcal{C}$.
 2. If none of $y_t(s_i)$ for all $i = 1, \dots, d$, are labelled as convective, then $t \in \mathcal{N}$.
-

the convective fields; note the difference in the scales of Figure 2.

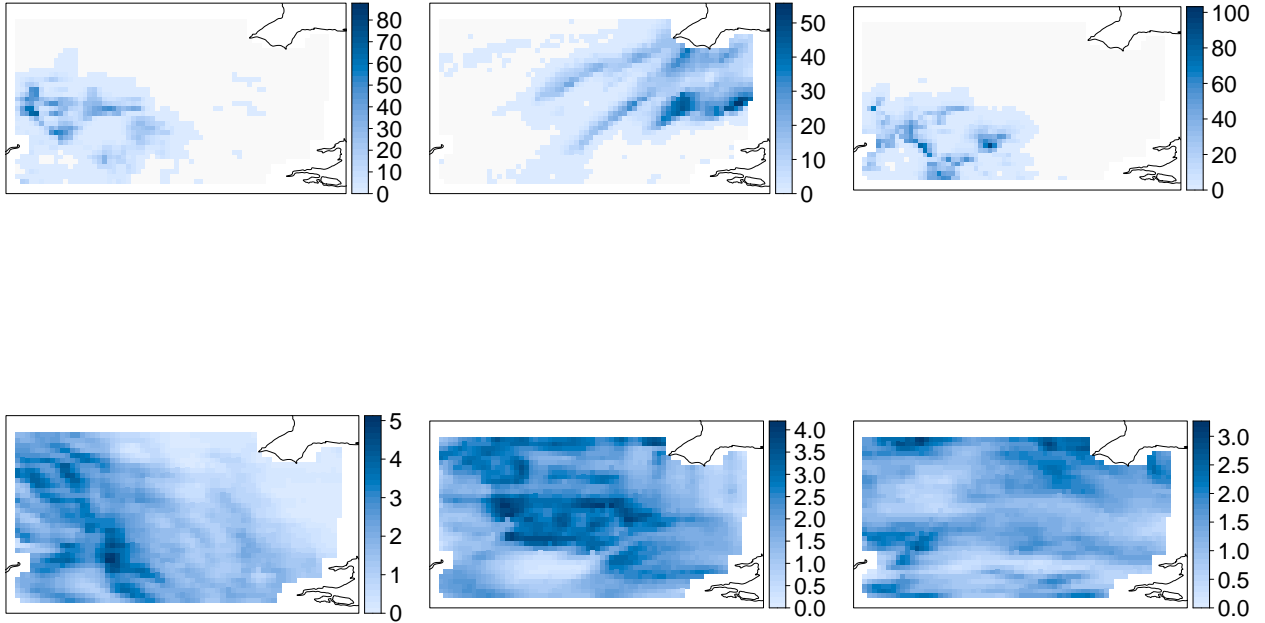


Figure 2: Observed extreme fields identified as convective (top) and non-convective (bottom) (mm/hr).

4.3 Marginal analysis

Marginal analysis is conducted by fitting the model described in Section 2.2 to each of the three datasets, i.e., convective, non-convective, and all. We set $\lambda = 0.995$ in (4) for all three processes and use a subset of 500 sites sampled randomly over \mathcal{S} to estimate $q_\lambda(s)$; whereas to estimate $p(s)$, $v(s)$ and ξ , we use all sampling locations. Figures S1-S3 in the Supplementary Material B (Richards et al., 2021b)

give estimates for the parameters of the marginal models and 20-year marginal return level estimates for $\{Y_{\mathcal{C}}(s)\}$, $\{Y_{\mathcal{N}}(s)\}$ and $\{Y_{\mathcal{E}}(s)\}$, respectively, with the latter being estimated for the specified process only. Different image colour scales are used across each panel and each of Figures S1-S3. We observe similar patterns in estimates of $p(s)$ and $q_{\lambda}(s)$ for each of the three processes, with $p(s)$ and $q_{\lambda}(s)$ decreasing and increasing with elevation, respectively.

There are differences between the estimates of $v(s)$ and the 20-year return levels for the three processes; for $Y_{\mathcal{C}}$ and $Y_{\mathcal{E}}$, we observe spatially smooth estimates of both, with larger values being found in the east of the domain (see Figures S1 and Figures S3) for $Y_{\mathcal{N}}$ both increase with elevation, indicating that the physical processes driving convection are only weakly affected by orthography, unlike frontal rain (see Figure S2). We observe much higher 20-year return levels for $Y_{\mathcal{C}}$ and $Y_{\mathcal{E}}$ than for $Y_{\mathcal{N}}$, which is consistent with their different physical properties. This property also holds for all larger return levels since the shape parameter estimates for $Y_{\mathcal{C}}$, $Y_{\mathcal{N}}$ and $Y_{\mathcal{E}}$, are 0.226, -0.075 and 0.287, respectively.

To assess the fit of the GPD GAM models, for each of $Y_{\mathcal{C}}$, $Y_{\mathcal{N}}$ and $Y_{\mathcal{E}}$ we present Q-Q plots of the marginal fits at five randomly sampled locations in Figures S4-S6, Appendix B, respectively. All figures show good individual fits for each of the processes. To evaluate the fit over all locations, we use a pooled Q-Q plot (Heffernan and Tawn, 2001), transforming all data onto standard exponential margins using the fitted model; these plots are also given in these figures. Again, we observe good fits for each process. Confidence intervals for the Q-Q plots are estimated using the following bootstrap procedure: we create 250 bootstrap samples of the data using the stationary bootstrap approach of Politis and Romano (1994) with expected block size of 48 hours. With $q_{\lambda}(s)$ treated as fixed across all samples, we then estimate $v(s)$ and ξ for each bootstrap sample. For the pooled diagnostic plot, we apply the marginal transformation to the original data using the 250 estimated GPD parameter sets.

4.4 Dependence modelling

We proceed by fitting the extremal dependence models described in Section 2.3 separately to $\{X_{\mathcal{C}}(s)\}$, $\{X_{\mathcal{N}}(s)\}$ and $\{X_{\mathcal{E}}(s)\}$. We use a different exceedance threshold, i.e., u in (5), for each process; the 96% quantile for $X_{\mathcal{C}}$ and the 99% quantile for $X_{\mathcal{E}}$ and $X_{\mathcal{N}}$. The thresholds were chosen so that the limiting assumptions in (5) were applicable; other choices were considered but these led to poorer inference on the extremal behaviour of spatial aggregates, which we quantified using the measures and diagnostics described in Section 4.5. Ideally, for $\{X_{\mathcal{E}}(s)\}$ we would set u such that

the number of observations used for inference was identical to the mixture approach to provide a fair comparison. However, we found that using such a threshold led to poorer inference for $\{X_{\mathcal{E}}(s)\}$, with significant evidence that assumptions in (5) fail for any lower threshold choice.

Inference is conducted using the stratified sampling regime described in Section 2.3. We use the same value of d_s for all three fitted models; we follow Richards et al. (2021a) and set $d_s = 5000$. Different values of h_{max} were also taken: $35km$ for $X_{\mathcal{E}}$ and $X_{\mathcal{C}}$ and $250km$ for $X_{\mathcal{N}}$, with the latter reflecting the long-range extremal dependence of $X_{\mathcal{N}}$. Inference for all three extremal dependence models was conducted using different sub-samples of sampling locations. For $X_{\mathcal{N}}$ we tried both forms of β , i.e., $\beta_{\mathcal{C}}$ and $\beta_{\mathcal{N}}$ in (7); with $\beta_{\mathcal{N}}$ giving a better fit, we present findings for this form only. Parameter estimates for all models are given in Supplementary Material A (Richards et al., 2021b). For $X_{\mathcal{E}}$ and $X_{\mathcal{C}}$, we found that fixing $\kappa_{\delta_4} = \kappa_{\beta_3} = 1$ and $\Delta = 0$ did not restrict the quality of either fit.

In Figure 3, we fix a conditioning site s_O in the centre of the domain and evaluate all dependence functions for each process at each pairwise anisotropic distance, i.e., $h(s_i, s_O)$ for $s_i \in \mathbf{s}$ and $i = 1, \dots, d$; these are then plotted against the great-circle distances in the original coordinate system, denoted $h_*(s_i, s_O)$. Figure 3 indicates that there are similarities within the extremal dependence structures of $X_{\mathcal{C}}$ and $X_{\mathcal{E}}$, as most of the functions are approximately equal with slight differences for μ and δ . In contrast, there are widely different estimated structures for the α and β functions for $X_{\mathcal{N}}$, with α decaying much slower and independence not being achieved for any pairs of sites within \mathcal{S} .

The estimate of $\Delta = 6.81$ given in Table S1 suggests that the process $X_{\mathcal{N}}$ is asymptotically dependent up to a distance of $6.81km$ in the anisotropic setting, corresponding to roughly $7.04km$ in the original coordinate system. Evidence of asymptotic dependence, even at short-range, has not been found previously using the spatial conditional extremes modelling approach, see e.g., Wadsworth and Tawn (2019), Huser and Wadsworth (2020), Simpson and Wadsworth (2021) and Shooter et al. (2021a). As extremal dependence is predominantly exhibited through the α function, this suggests that extreme realisations of $\{X_{\mathcal{N}}(s) : s \in \mathcal{S}\}$ are much smoother than extreme events drawn from the other two processes, which agrees with our understanding of convective and non-convective precipitation. Keef et al. (2013) identify additional constraints for the Heffernan and Tawn (2004) framework, which in the spatial context correspond to $\beta(h) = 0$ whenever $\alpha(h) = 1$; our fitted model breaks this constraint with $0 < \beta < 0.003$ for $0 < h \leq \Delta$, but this minor deviation is not problematic.

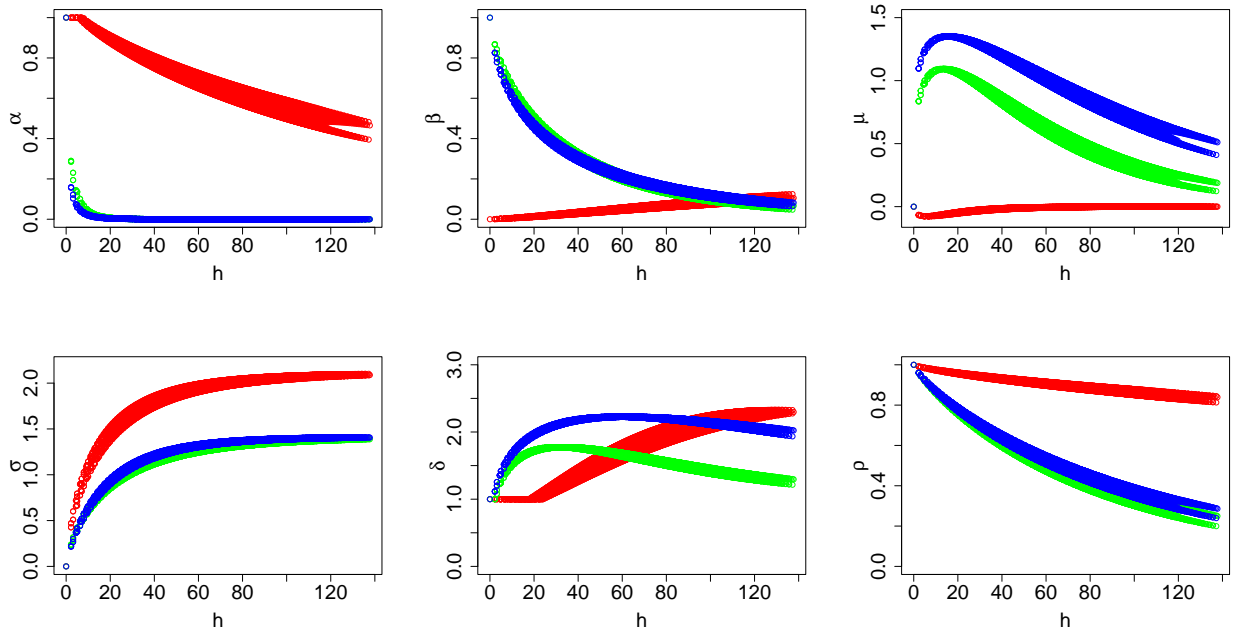


Figure 3: Estimates of extremal dependence functions evaluated at $h(s_i, s_O)$ for $i = 1, \dots, d$, i.e., anisotropic distances, against great-circle distances $h := h_*(s_i, s_O)$, which are given in *km*. The conditioning site s_O is in the centre of the spatial domain \mathcal{S} . The colours correspond to the estimates for the different spatial processes; these are green, red and blue for $\{X_{\mathcal{C}}(s)\}$, $\{X_{\mathcal{N}}(s)\}$ and $\{X_{\mathcal{E}}(s)\}$, respectively.

To compare the model fits, i.e., $Y_{\mathcal{C}}$, $Y_{\mathcal{N}}$ and $Y_{\mathcal{E}}$, we propose the following diagnostic that we present for a generic $\{Y(s)\}$ process. We investigate how the “conditional process” $\{Y(s) : s \in \mathcal{S} | (Y(s_O) = v^{(l)})\}$ changes with distance $h_*(s, s_O)$ for $s, s_O \in \mathcal{S}$, where $v^{(l)}$ denotes the l -year return level for $Y(s_O)$. Figure 4 gives point-wise estimates for the median, and the 2.5% and 97.5% marginal quantiles, for $l = 1$ and 50 for the conditional process; these are obtained from 50000 realisations from the fitted model. To achieve the largest possible distances, s_O is chosen to be on the boundary of \mathcal{S} and to ease comparison, we consider a transect of points in \mathcal{S} only. We take into account the respective length of observation periods when evaluating the respective l -year return levels, e.g., for $Y_{\mathcal{C}}$ we take $v^{(l)} = F_{Y_{\mathcal{C}}(s_O)}^{-1}(1 - 1/(l \times |\mathcal{C}|/20))$ and similarly for $Y_{\mathcal{N}}$ and $Y_{\mathcal{E}}$. The diagnostics for $Y_{\mathcal{C}}$ and $Y_{\mathcal{E}}$ are almost identical, with $v_{\mathcal{E}}^{(l)}$ and $v_{\mathcal{C}}^{(l)}$ approximately equal, and with the conditional medians of the respective processes both decaying quickly with distance. For $Y_{\mathcal{N}}$, the conditional median decays fairly slowly, with non-zero values at even the largest distances.

Figure 5 presents realisations of $\{Y(s) : s \in \mathcal{S} | (Y(s_O) > v)\}$ for $Y_{\mathcal{C}}$ and $Y_{\mathcal{N}}$, where $v = F_L^{-1}(0.99)$

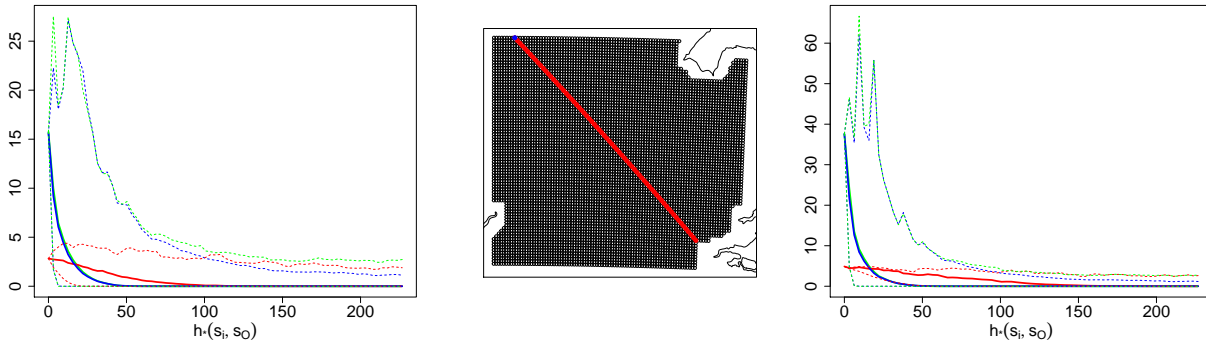


Figure 4: Summary statistics for $\{Y(s) : s \in \mathcal{S}\} | (Y(s_O) = v^{(l)})$ against distance $h_*(s, s_O)$ with $l = 1$ and $l = 50$ in the left and right plots, respectively; the process is considered along a transect of points only. Solid lines correspond to estimates for conditional medians, dashed lines denote 95% confidence intervals. Lines are coloured green, red and blue for Y_C , Y_N and Y_E , respectively. Centre: red and blue points denote the transect and s_O , respectively.

and each s_O was uniformly sampled over \mathcal{S} , with their locations identified; similar plots are given for Y_E in Figure S7, Supplementary Materials (Richards et al., 2021b). There are similarities for $Y_C(s)$ and $Y_E(s)$, with characteristics we anticipated for convective rainfall, i.e., high intensity, spatially localised events with a large proportion of the domain \mathcal{S} being dry. In contrast, Y_N produces events that are much smoother spatially, cover a much large area, and are lower in their intensity.

4.5 Inference on spatial aggregates

For each process, we draw 5.5×10^5 realisations using Algorithm 1, b' being increased until the estimated quantiles of $\bar{R}_{\mathcal{A}}$ were stable. For Y_C and Y_E , we used $b' = 8b$; for Y_N , $b' = 12b$. Regions $\mathcal{S}_s, \mathcal{A}_c$ and \mathcal{A} , described in Section 3.2, are illustrated in Figure 1; \mathcal{A} and \mathcal{S}_s are not changed over the processes, but we take $\mathcal{A}_c = \phi$ for Y_C and Y_E and for Y_N we create \mathcal{A}_c using the heuristic described in Section 3.2, with $\mathcal{A}_c \setminus \mathcal{S}_s$ illustrated by the purple points in Figure 1. Using these regions, we create samples of $\{Y_{\mathcal{M}}(s) : s \in \mathcal{S}_s\}$ for different regions \mathcal{A} (see Figure 1) by drawing from $\{Y_C(s) : s \in \mathcal{S}_s\}$ and $\{Y_N(s) : s \in \mathcal{S}_s\}$ with estimated probability p_C and $1 - p_C$, respectively.

Recall that $\bar{R}_{\mathcal{M}, \mathcal{A}}$ denote samples from $\bar{R}_{\mathcal{A}}$ created using our new modelling approach and $\bar{R}_{\mathcal{E}, \mathcal{A}}$ denote samples using the single process approach of Richards et al. (2021a). To compare mixture and non-mixture approaches, we present Q-Q plots in Figures 6 and S8 (Supplementary Materials (Richards et al., 2021b)) for spatial aggregates. In Figure S8, we assess the fit of individual mixture components Y_C and Y_N by using Q-Q plots of the variables $\bar{R}_{C, \mathcal{A}} := |\mathcal{A}|^{-1} \int_{\mathcal{A}} Y_C(s) ds$ and $\bar{R}_{N, \mathcal{A}} := |\mathcal{A}|^{-1} \int_{\mathcal{A}} Y_N(s) ds$.

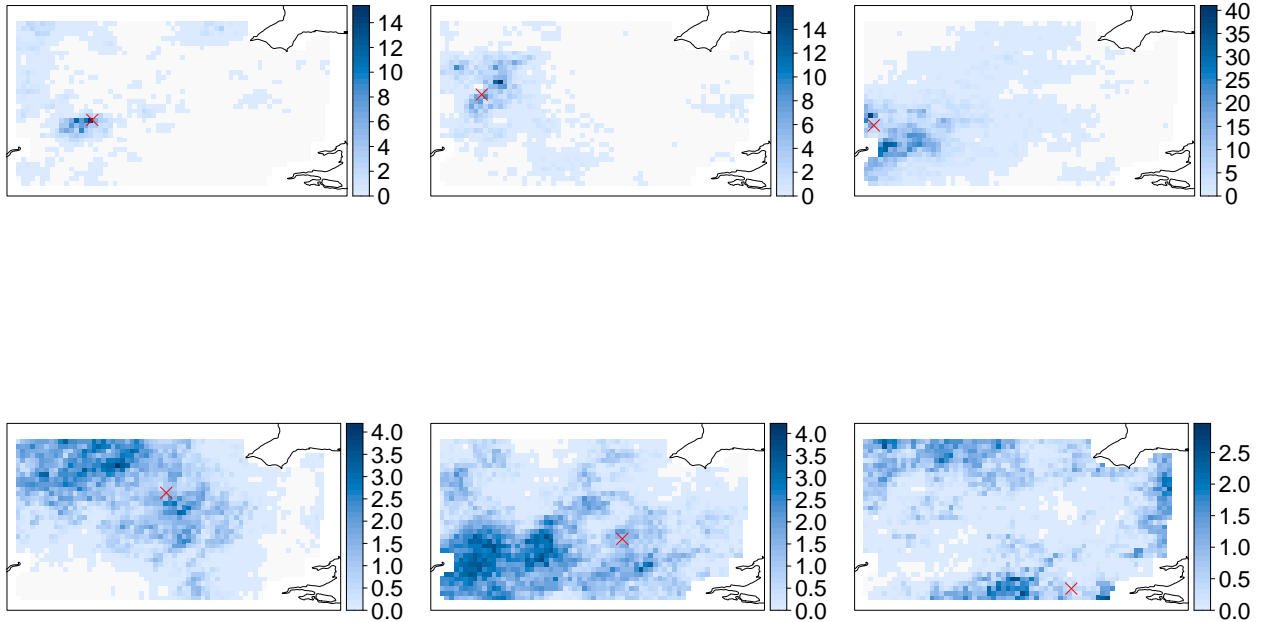


Figure 5: Extreme precipitation fields (mm/hr). Realisations from the fitted models for $\{Y(s) : s \in \mathcal{S} | (Y(s_0) > v)\}$, with the top and bottom rows corresponding to Y_C and Y_N , respectively. The conditioning sites s_0 are given by the red crosses. Scales differ within each panel and row.

For Figure 6, we compare Q-Q plots for both $\bar{R}_{\mathcal{M},\mathcal{A}}$ and $\bar{R}_{\mathcal{E},\mathcal{A}}$. Point-wise confidence interval estimates for the quantiles on these figures are created using a bootstrap technique. Specifically, we obtain a sample of 50 parameter estimates for each of model X_C and X_N by first applying a stationary bootstrap (Politis and Romano, 1994) to observations of the process with expected block size of 48 hours, and then fitting the extremal dependence model of Section 2.3, i.e., with the same h_{max} and d_s , but using different triples of sampling locations. For each of the 50 parameter estimates for X_C and X_N , we draw 5.5×10^5 realisations of $\{Y_{\mathcal{M}}(s) : s \in \mathcal{A}_c\}$, with \mathcal{A}_c and \mathcal{S}_s consistent across parameter estimates. Our implementation fixed p_c as we believe that incorporating its uncertainty does not justify the computational expense given the precision with which p_c is estimated.

In Figures 6 and S8, we observe good fits for all components of both modelling approaches, with slight underestimation for the smaller quantiles of $\bar{R}_{\mathcal{N},\mathcal{A}}$. It appears that $\bar{R}_{\mathcal{M},\mathcal{A}}$ provides slightly better fits than the corresponding $\bar{R}_{\mathcal{E},\mathcal{A}}$ for most of the tail, particularly for the largest regions, numbered 3

and 4; indicating an improvement over the approach of Richards et al. (2021a). To help understand these observed differences in fit, we estimate the proportion $p_{\mathcal{M}}(v^{(l)}, \mathcal{A})$ of non-convective events that contribute to $\bar{R}_{\mathcal{M}, \mathcal{A}} > v^{(l)}$, where here $v^{(l)}$ denotes the 99% and 99.5% quantile of the simulated $\bar{R}_{\mathcal{M}, \mathcal{A}}$. The proportion $p_{\mathcal{M}}(v^{(l)}, \mathcal{A})$ increases with the size of \mathcal{A} ; for the 99% quantile, $p_{\mathcal{M}}(v^{(l)}, \mathcal{A})$ increases from 0.029 to 0.052 for the smallest and largest regions, respectively, and for the 99.5% quantile, the values increases from 0.004 to 0.040. Neither the models for $\bar{R}_{\mathcal{M}, \mathcal{A}}$ nor $\bar{R}_{\mathcal{E}, \mathcal{A}}$ are able to capture the very largest empirical quantiles when \mathcal{A} is the smallest region, region 1. This discrepancy was caused by two, potentially spurious (Whitall, 2021), events that produced large values for the average over region 1, at consecutive hours; in Section 5 we discuss extensions to the model that may help to capture these events.

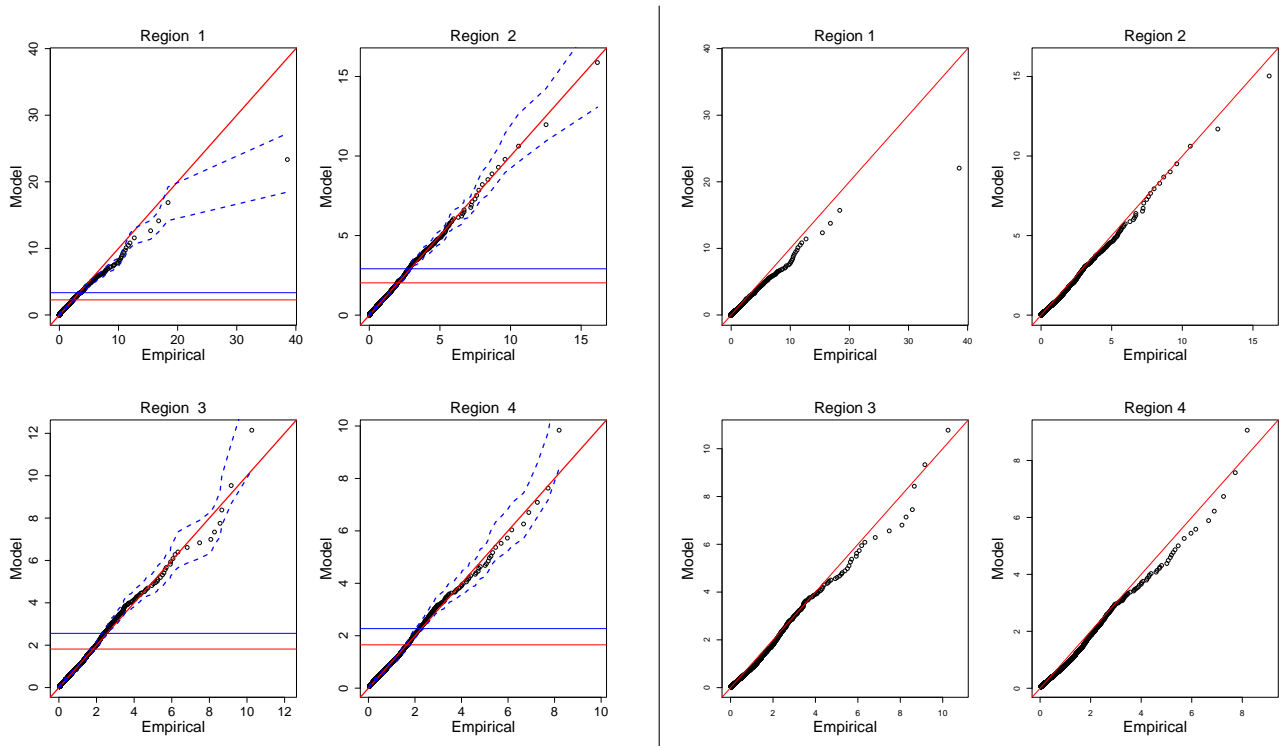


Figure 6: Q-Q plots for the model, and empirical, aggregates of regions of increasing size. Left: $\bar{R}_{\mathcal{M}, \mathcal{A}}$, right: $\bar{R}_{\mathcal{E}, \mathcal{A}}$, Probabilities range from 0.8 to a value corresponding to the respective 20 year return level. Blue dashed lines denote point-wise 95% quantile estimates. Regions 1-4 correspond to those illustrated in Figure 1. The blue and red horizontal lines denote the 99% and 99.5% quantiles of the respective simulated aggregates.

To better quantify our assertion that model \mathcal{M} fits better than model \mathcal{E} , we present a comparison using a metric adapted from a measure of Varty et al. (2021). Let $Q(p; Z) : [0, 1] \rightarrow \mathbb{R}_+$ denote the sample p -th quantile of random variable Z and $\tilde{R}_{\mathcal{A}}$ denote the observed spatial aggregate. Then

we define measures of the expected deviance in the Q-Q plot for Z against $\tilde{R}_{\mathcal{A}}$ from the line $y = x$,

$$\Lambda_i(Z) = \frac{1}{m} \sum_{j=1}^m |Q(p_j; Z) - Q(p_j; \tilde{R}_{\mathcal{A}})|^i, \quad \text{for } i = 1, 2, \quad (14)$$

described through the mean absolute, and mean squared, distances in Λ_1 and Λ_2 , respectively, where $\{0 < p_1 < \dots < p_m < 1\}$ is a grid of m ($m \geq 2$) equally spaced values with $p_m = 1 - (p_2 - p_1)$. As our interest lines in the upper-tails of $\tilde{R}_{\mathcal{A}}$, we set p_1 close to one. We evaluate Λ_1 and Λ_2 for $Z := \bar{R}_{\mathcal{M},\mathcal{A}}$ and $Z := \bar{R}_{\mathcal{E},\mathcal{A}}$, and for each region \mathcal{A} illustrated in Figure 1, with $p_1 = 0.99$ and $m = 432$, i.e., the number of observations of $\tilde{R}_{\mathcal{A}}$ that exceed the 0.99-quantile. These goodness-of-fit diagnostics are given in Table 1, with smaller values indicating a best fit under that metric, with our approach providing better fits for all four regions.

	\mathcal{A}			
	1	2	3	4
$\Lambda_1(\bar{R}_{\mathcal{M},\mathcal{A}})$	0.37	0.09	0.14	0.09
$\Lambda_1(\bar{R}_{\mathcal{E},\mathcal{A}})$	0.65	0.21	0.15	0.18
$\Lambda_2(\bar{R}_{\mathcal{M},\mathcal{A}})$	1.09	0.02	0.04	0.01
$\Lambda_2(\bar{R}_{\mathcal{E},\mathcal{A}})$	1.25	0.06	0.05	0.05

Table 1: Estimates of aggregate diagnostics Λ_1 and Λ_2 defined in (14) to 2 d.p.

5 Discussion

We have presented a simple but effective mixture model extension of the approach proposed by Richards et al. (2021a) for modelling the extremes of spatial aggregates of precipitation over a wide range of spatial scales. We classify observed fields as being either convective or non-convective, fit separate spatial models to each dataset and then simulate from both models and combine samples to explore the upper-tail behaviour of $\tilde{R}_{\mathcal{A}}$, see (1). Our mixture modelling approach was compared against an approach where the mixture structure is ignored and we found that the former was able to better capture the extremal behaviour of aggregates over very large spatial regions. We now discuss some further extensions that can be made to improve the model.

In Section 4.5, we identified two consecutive convective events that provided the two largest values of the empirical $\tilde{R}_{\mathcal{A}}$ over the smallest aggregate region \mathcal{A} , denoted region 1; neither the model for $\bar{R}_{\mathcal{M},\mathcal{A}}$ nor $\bar{R}_{\mathcal{E},\mathcal{A}}$ were able to capture the characteristics of these two events. The consecutive nature of the

values suggests that there may be a temporal aspect to the data that we cannot currently capture with the model. The data themselves are aggregates of continuous-in-time precipitation over a temporal interval of one hour and a spatial grid-box. Hence, two spatially identical storms can produce different hourly values simply by moving at different speeds through a grid-box. Potential model extensions would incorporate the speed of a storm as a covariate in the model or build a conditional spatial-temporal model (Simpson and Wadsworth, 2021) adapted for precipitation.

We classified entire observed fields as convective or not regardless of the amount of convective rainfall properties across \mathcal{S} , or the presence/proportion of non-convective rainfall within the same spatial domain. The classification of the whole field into one of two processes appears to work well as we observe distinctly different structures for the two identified components. A more realistic approach is to accommodate spatial mixing of convective and non-convective rainfall across \mathcal{S} within a single field. This may require modelling of extremal dependence between rain types and a framework for simulating different types of event within the same region.

The classification technique is deterministic and so improvements may be achieved by adopting a more probabilistic approach with labelling of mixture components conducted within inference. In this vein, Tendijck et al. (2021) have developed mixture models in a conditional extremes setting by allowing the α and β functions to change with the mixture component, but only in a bivariate context. For the residual process $Z(s|s_O)$, a Dirichlet mixture of Gaussian processes (see Duan et al. (2007)) could be used, rather than a single process. This would have the added benefit of the model not being limited to only two mixture components. Instead, a number of mixture components could be used, each with their own dependence structure. In the context of modelling spatial extremes, Hazra and Huser (2021) advocate the use of Dirichlet mixtures of Student- t processes.

Acknowledgements

Richards and Tawn gratefully acknowledge funding through the STOR-i Doctoral Training Centre and Engineering and Physical Sciences Research Council (grant EP/L015692/1). This publication is based upon work supported by the King Abdullah University of Science and Technology (KAUST) Office of Sponsored Research (OSR) under Award No. OSR-CRG2020-4394. Brown was supported by the Met Office Hadley Centre Climate Programme funded by BEIS and Defra.

References

- Berg, P., Moseley, C., and Haerter, J. O. (2013). Strong increase in convective precipitation in response to higher temperatures. *Nature Geoscience*, 6(3):181–185.
- Brown, S. J. (2018). The drivers of variability in UK extreme rainfall. *International Journal of Climatology*, 38(S1):e119–e130.
- Catto, J. L. and Pfahl, S. (2013). The importance of fronts for extreme precipitation. *Journal of Geophysical Research: Atmospheres*, 118(19):10–791.
- Coles, S. G. (2001). *An Introduction to Statistical Modeling of Extreme Values*. Springer series in Statistics. Springer-Verlag, London.
- Coles, S. G. and Tawn, J. A. (1996). Modelling extremes of the areal rainfall process. *Journal of the Royal Statistical Society. Series B (Methodological)*, 58(2):329–347.
- Cooley, D., Nychka, D., and Naveau, P. (2007). Bayesian spatial modeling of extreme precipitation return levels. *Journal of the American Statistical Association*, 102(479):824–840.
- Cooley, D. and Sain, S. R. (2010). Spatial hierarchical modeling of precipitation extremes from a regional climate model. *Journal of Agricultural, Biological, and Environmental Statistics*, 15(3):381–402.
- de Fondeville, R. and Davison, A. C. (2020). Functional peaks-over-threshold analysis. *arXiv preprint arXiv:2002.02711*.
- Duan, J. A., Guindani, M., and Gelfand, A. E. (2007). Generalized spatial Dirichlet process models. *Biometrika*, 94(4):809–825.
- Fasiolo, M., Wood, S. N., Zaffran, M., Nedellec, R., and Goude, Y. (2021). Fast calibrated additive quantile regression. *Journal of the American Statistical Association*, 116(535):1402–1412.
- Gregersen, I. B., Sørup, H. J. D., Madsen, H., Rosbjerg, D., Mikkelsen, P. S., and Arnbjerg-Nielsen, K. (2013). Assessing future climatic changes of rainfall extremes at small spatio-temporal scales. *Climatic Change*, 118(3):783–797.

- Hazra, A. and Huser, R. (2021). Estimating high-resolution Red Sea surface temperature hotspots, using a low-rank semiparametric spatial model. *The Annals of Applied Statistics*, 15(2):572 – 596.
- Heffernan, J. E. and Tawn, J. A. (2001). Extreme value analysis of a large designed experiment: A case study in bulk carrier safety. *Extremes*, 4(4):359–378.
- Heffernan, J. E. and Tawn, J. A. (2004). A conditional approach for multivariate extreme values (with discussion). *Journal of the Royal Statistical Society: Series B (Methodology)*, 66(3):497–546.
- Houze Jr, R. A. (1997). Stratiform precipitation in regions of convection: A meteorological paradox? *Bulletin of the American Meteorological Society*, 78(10):2179–2196.
- Huser, R. and Wadsworth, J. L. (2020). Advances in statistical modeling of spatial extremes. *Wiley Interdisciplinary Reviews: Computational Statistics*, page e1537.
- Institute of Hydrology (1999). *Flood Estimation Handbook*. IH, Wallingford, UK.
- Joe, H. (1997). *Multivariate Models and Multivariate Dependence Concepts*. CRC Press.
- Keef, C., Papastathopoulos, I., and Tawn, J. A. (2013). Estimation of the conditional distribution of a multivariate variable given that one of its components is large: Additional constraints for the Heffernan and Tawn model. *Journal of Multivariate Analysis*, 115:396–404.
- Kendon, E. J., Roberts, N. M., Senior, C. A., and Roberts, M. J. (2012). Realism of rainfall in a very high-resolution regional climate model. *Journal of Climate*, 25(17):5791–5806.
- Lowe, J., Bernie, D., Bett, P., Bricheno, L., Brown, S., Calvert, D., Clark, R., Karen, Eagle, Edwards, T., Fosser, G., Maisey, P., McInnes, R., Mcsweeney, C., Yamazaki, K., and Belcher, S. (2018). UKCP18 science overview report. *Met Office Hadley Centre: Exeter, UK*.
- Politis, D. N. and Romano, J. P. (1994). The stationary bootstrap. *Journal of the American Statistical Association*, 89(428):1303–1313.
- Richards, J., Tawn, J. A., and Brown, S. (2021a). Modelling extremes of spatial aggregates of precipitation using conditional methods. *arXiv preprint arXiv:2102.10906*.
- Richards, J., Tawn, J. A., and Brown, S. (2021b). Supplement to “Joint estimation of extreme precipitation aggregates at different spatial scales through mixture modelling”.

- Roberts, N. and Kendon, E. (2020). Personal communication.
- Saunders, K., Stephenson, A. G., Taylor, P. G., and Karoly, D. (2017). The spatial distribution of rainfall extremes and the influence of El Niño Southern Oscillation. *Weather and Climate Extremes*, 18:17–28.
- Schroeder, K., Kirchengast, G., and O, S. (2018). Strong dependence of extreme convective precipitation intensities on gauge network density. *Geophysical Research Letters*, 45(16):8253–8263.
- Shooter, R., Ross, E., Ribal, A., Young, I., and Jonathan, P. (2021a). Spatial dependence of extreme seas in the North East Atlantic from satellite altimeter measurements. *Environmetrics*, 32(4):e2674.
- Shooter, R., Ross, E., Tawn, J. A., and Jonathan, P. (2019). On spatial conditional extremes for ocean storm severity. *Environmetrics*, 30(6):e2562.
- Shooter, R., Tawn, J. A., Ross, E., and Jonathan, P. (2021b). Basin-wide spatial conditional extremes for severe ocean storms. *Extremes*, 24(2):241–265.
- Simpson, E. S., Opitz, T., and Wadsworth, J. L. (2021). High-dimensional modeling of spatial and spatio-temporal conditional extremes using INLA and the SPDE approach. *arXiv e-prints*, arXiv:2011.04486.
- Simpson, E. S. and Wadsworth, J. L. (2021). Conditional modelling of spatio-temporal extremes for Red Sea surface temperatures. *Spatial Statistics*, 41:100482.
- Tawn, J. A., Shooter, R., Towe, R., and Lamb, R. (2018). Modelling spatial extreme events with environmental applications. *Spatial Statistics*, 28:39–58.
- Tendijck, S., Eastoe, E., Tawn, J., Randell, D., and Jonathan, P. (2021). Modelling the extremes of bivariate mixture distributions with application to oceanographic data. To appear in the Journal of the American Statistical Association, DOI: 10.1080/01621459.2021.1996379.
- Thibaud, E., Mutzner, R., and Davison, A. C. (2013). Threshold modeling of extreme spatial rainfall. *Water Resources Research*, 49(8):4633–4644.
- Varty, Z., Tawn, J. A., Atkinson, P. M., and Bierman, S. (2021). Inference for extreme earthquake magnitudes accounting for a time-varying measurement process. *arXiv preprint arXiv:2102.00884*.

- Wadsworth, J. L. and Tawn, J. A. (2019). Higher-dimensional spatial extremes via single-site conditioning. *arXiv e-prints*, arXiv:1912.06560.
- Whitall, M. (2021). Personal communication.
- Wood, S. (2006). *Generalized Additive Models: An Introduction with R*. Chapman & Hall/CRC Texts in Statistical Science. Taylor & Francis.
- Youngman, B. D. (2019). Generalized additive models for exceedances of high thresholds with an application to return level estimation for U.S. wind gusts. *Journal of the American Statistical Association*, 114(528):1865–1879.
- Zheng, F., Thibaud, E., Leonard, M., and Westra, S. (2015). Assessing the performance of the independence method in modeling spatial extreme rainfall. *Water Resources Research*, 51(9):7744–7758.

Supplementary Material

A Model parameter estimates

Tables S1-S3 give the estimates and standard errors for the extremal dependence model parameters. Note that those parameters without standard errors were treated as fixed in model inference.

Table S1: Parameter estimates (standard errors) to 2 d.p. for $X_{\mathcal{N}}$.

$\alpha_{\mathcal{N}}(h)$			$\beta_{\mathcal{N}}(h)$		
κ_{α_1}	κ_{α_2}	Δ	κ_{β_1}	κ_{β_2}	κ_{β_3}
170.07 (14.48)	0.87 (0.06)	6.81 (3.71)	0.12 (0.04)	1.36 (0.37)	256.00 (1.34)

$\mu_{\mathcal{N}}(h)$			$\sigma_{\mathcal{N}}(h)$		
κ_{μ_1}	κ_{μ_2}	κ_{μ_3}	κ_{σ_1}	κ_{σ_2}	κ_{σ_3}
-0.06 (0.02)	0.40 (0.54)	15.50 (3.26)	16.79 (2.59)	0.73 (0.09)	2.11 (0.14)

$\delta_{\mathcal{N}}(h)$			
κ_{δ_1}	κ_{δ_2}	κ_{δ_3}	κ_{δ_4}
1.84×10^{-3} (1.93×10^{-3})	1.65 (0.14)	90.57 (7.84)	0.28 (0.21)

$\rho_{\mathcal{N}}(h)$		$h_{\mathcal{N}}(s, s_0)$	
κ_{ρ_1}	κ_{ρ_2}	θ	L
1496.36 (352.88)	0.36 (0.02)	-0.32 (0.08)	1.00 (0.03)

Table S2: Parameter estimates (standard errors) to 2 d.p. for $X_{\mathcal{C}}$.

$\alpha_{\mathcal{C}}(h)$			$\beta_{\mathcal{C}}(h)$			$\mu_{\mathcal{C}}(h)$		
κ_{α_1}	κ_{α_2}	Δ	κ_{β_1}	κ_{β_2}	κ_{β_3}	κ_{μ_1}	κ_{μ_2}	κ_{μ_3}
1.60 (1.35)	0.64 (0.11)	0.00	32.49 (4.64)	0.73 (0.09)	1.00	0.70 (0.18)	0.28 (0.11)	47.56 (19.83)

$\sigma_{\mathcal{C}}(h)$		$\delta_{\mathcal{C}}(h)$			
κ_{σ_1}	κ_{σ_2}	κ_{δ_1}	κ_{δ_2}	κ_{δ_3}	κ_{δ_4}
20.87 (2.97)	0.76 (0.03)	0.77 (0.06)	0.32 (0.05)	57.90 (8.94)	1.00

$\rho_{\mathcal{C}}(h)$		$h_{\mathcal{C}}(s, s_0)$	
κ_{ρ_1}	κ_{ρ_2}	θ	L
104.81 (17.54)	0.41 (0.01)	-0.15 (0.02)	0.97 (0.01)

Table S3: Parameter estimates (standard errors) to 2 d.p. for $X_{\mathcal{E}}$.

$\alpha_{\mathcal{E}}(h)$			$\beta_{\mathcal{E}}(h)$			$\mu_{\mathcal{E}}(h)$		
κ_{α_1}	κ_{α_2}	Δ	κ_{β_1}	κ_{β_2}	κ_{β_3}	κ_{μ_1}	κ_{μ_2}	κ_{μ_3}
0.65	0.50	0.00	30.28	0.63	1.00	0.96	1.19	81.83

$\sigma_{\mathcal{E}}(h)$		$\delta_{\mathcal{E}}(h)$				$\rho_{\mathcal{E}}(h)$		$h_{\mathcal{E}}(s, s_O)$	
κ_{σ_1}	κ_{σ_2}	κ_{δ_1}	κ_{δ_2}	κ_{δ_3}	κ_{δ_4}	κ_{ρ_1}	κ_{ρ_2}	θ	L
18.62	0.85	0.88	0.29	136.26	1.00	121.52	0.40	-0.14	0.98

B Supplementary Figures

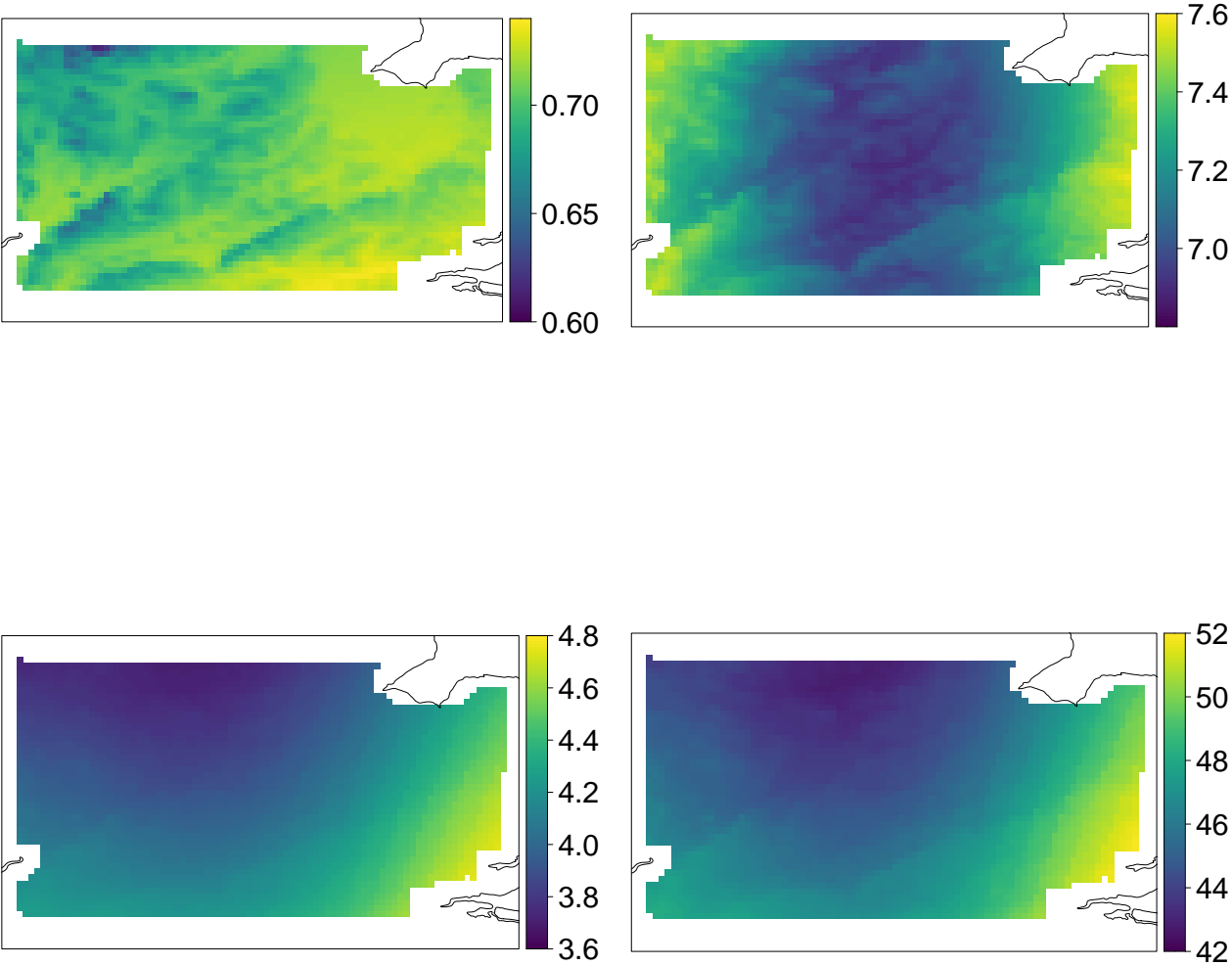


Figure S1: Spatially smoothed marginal distribution parameter estimates for $\{Y_C(s)\}$, i.e., convective rainfall. Top-left: $\hat{p}(s)$, top-right: $\hat{q}(s)$, bottom-left: $\hat{v}(s)$, bottom-right: 20-year return level estimate.

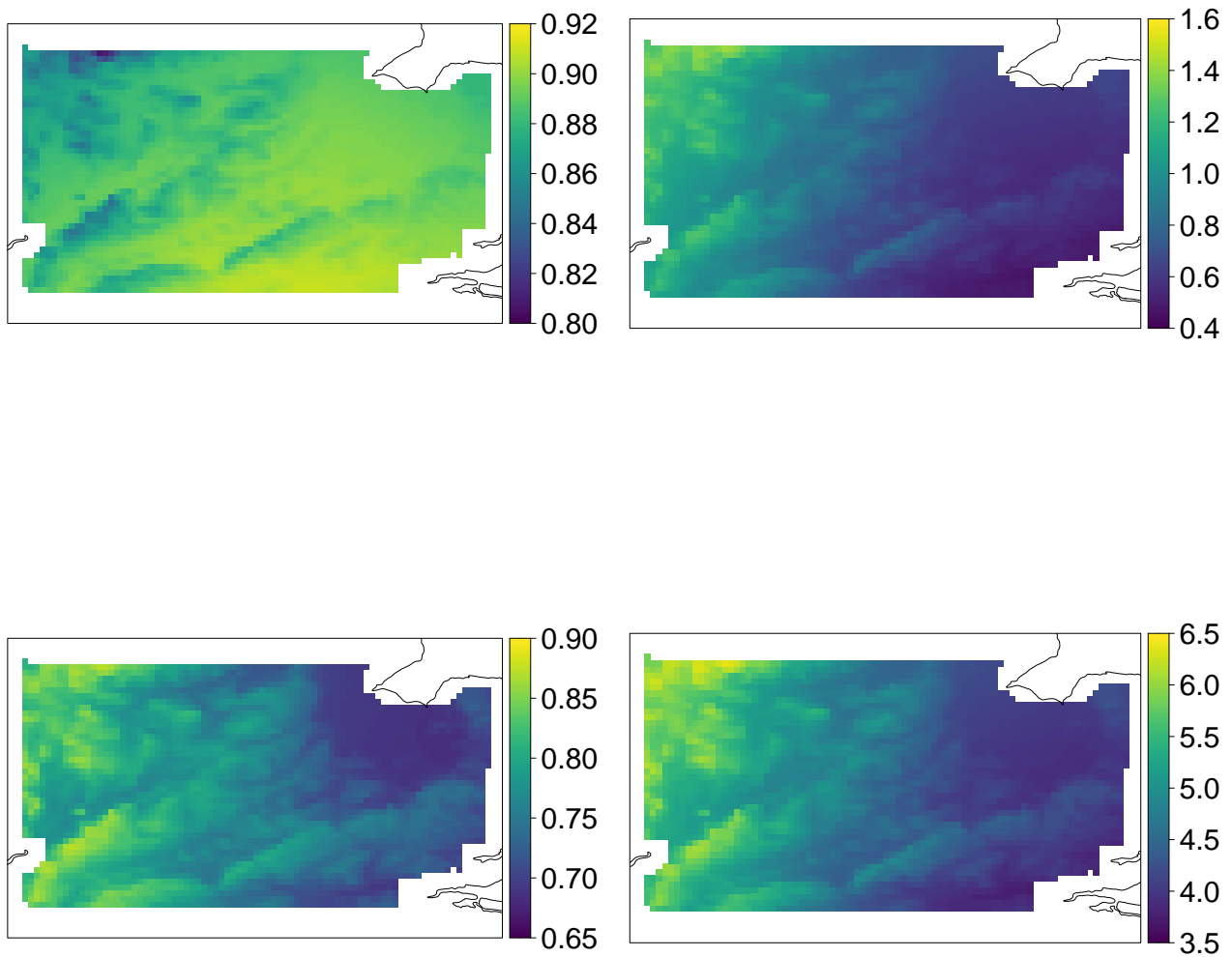


Figure S2: Spatially smoothed marginal distribution parameter estimates for $\{Y_{\mathcal{N}}(s)\}$, i.e., non-convective rainfall. Top-left: $\hat{p}(s)$, top-right: $\hat{q}(s)$, bottom-left: $\hat{v}(s)$, bottom-right: 20-year return level estimate.

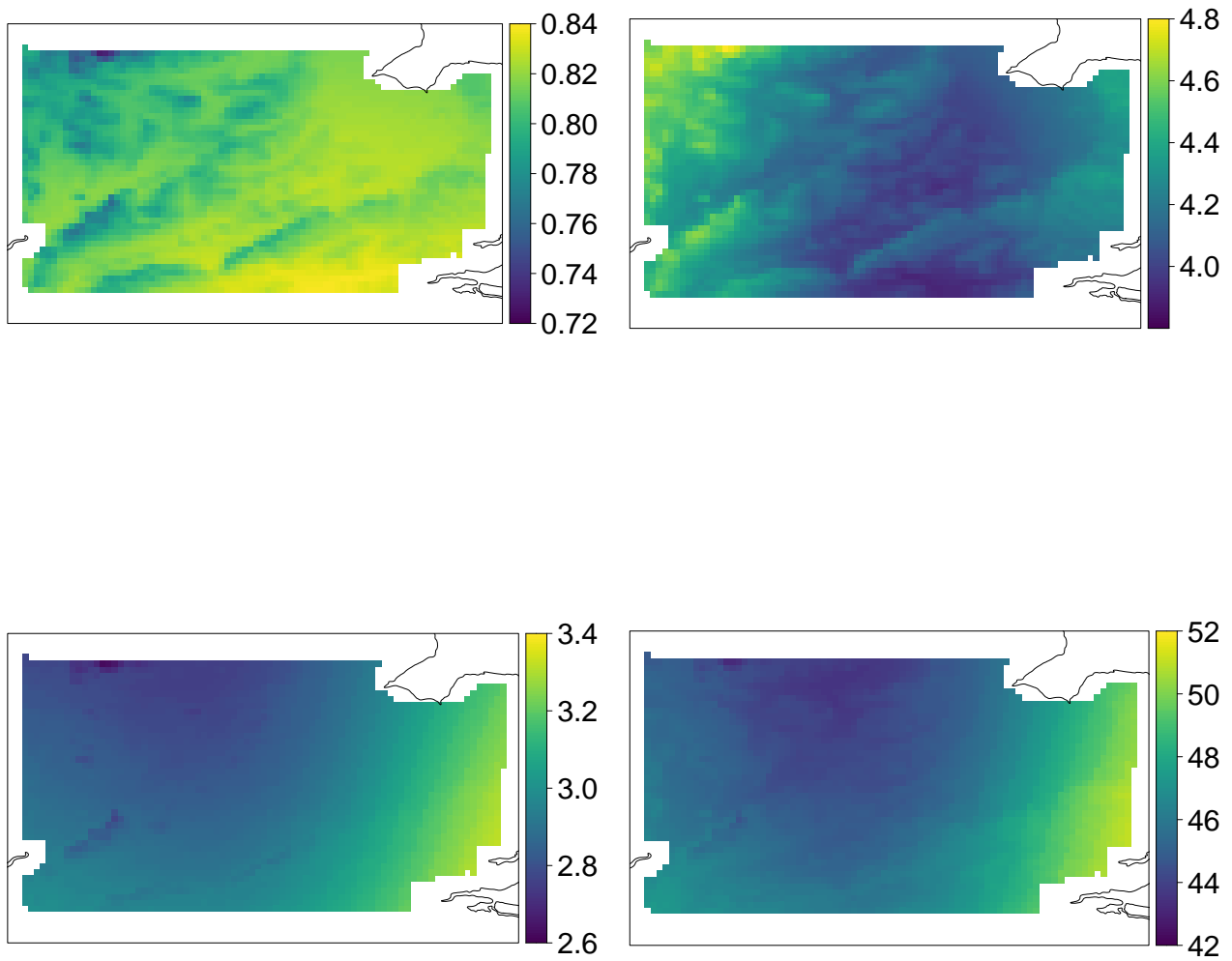


Figure S3: Spatially smoothed marginal distribution parameter estimates for $\{Y_{\mathcal{E}}(s)\}$, i.e., all rainfall. Top-left: $\hat{p}(s)$, top-right: $\hat{q}(s)$, bottom-left: $\hat{v}(s)$, bottom-right: 20-year return level estimate.

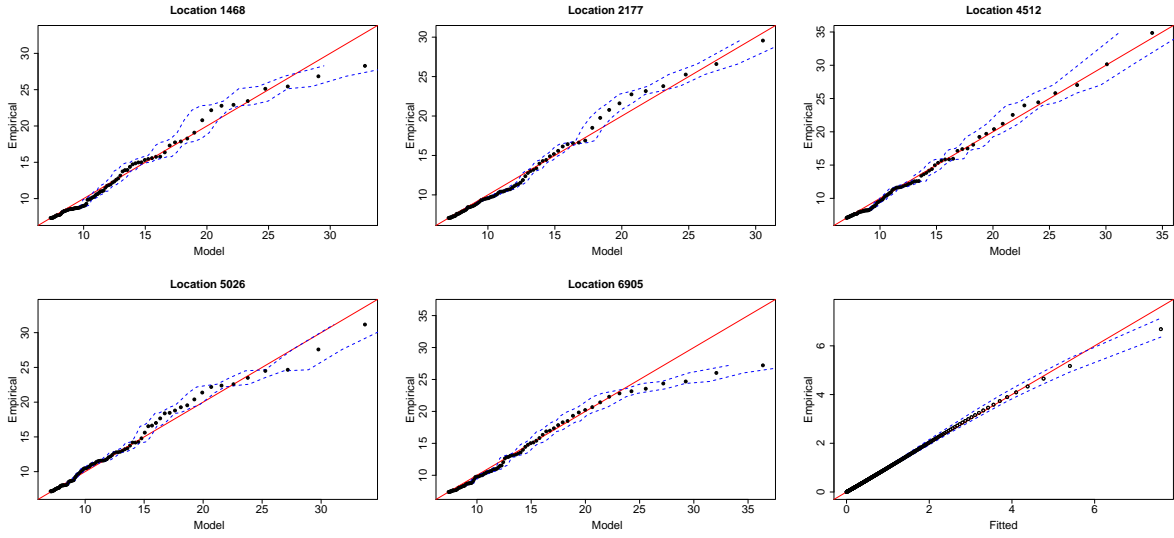


Figure S4: Q-Q plots for the GPD GAM fits for $\{Y_C(s)\}$ at five randomly sampled sites in \mathcal{S} . Bottom-right: Q-Q plot for pooled marginal transformation over all sites to standard exponential margins. The 95% confidence intervals are given by the blue dashed lines.

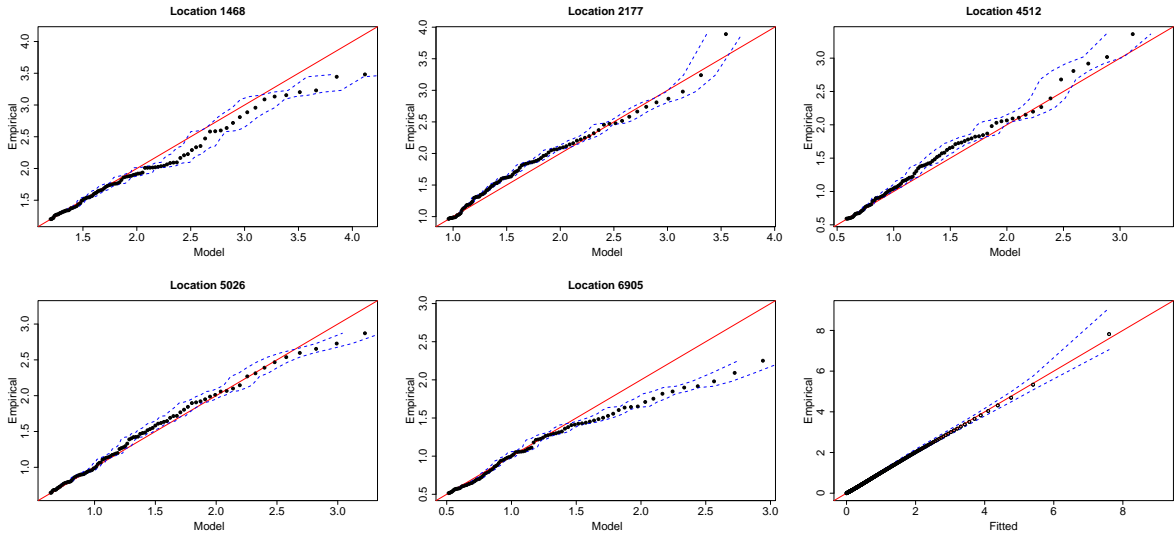


Figure S5: Q-Q plots for the GPD GAM fits for $\{Y_N(s)\}$ at five randomly sampled sites in \mathcal{S} . Bottom-right: Q-Q plot for pooled marginal transformation over all sites to standard exponential margins. The 95% confidence intervals are given by the blue dashed lines.

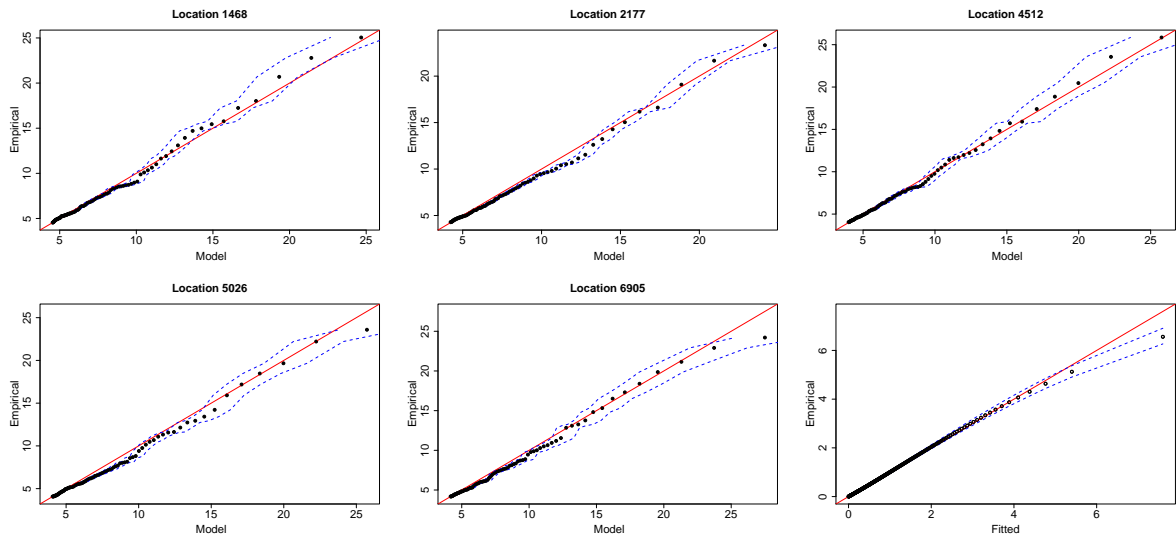


Figure S6: Q-Q plots for the GPD GAM fits for $\{Y_{\mathcal{E}}(s)\}$ at five randomly sampled sites in \mathcal{S} . Bottom-right: Q-Q plot for pooled marginal transformation over all sites to standard exponential margins. The 95% confidence intervals are given by the blue dashed lines.

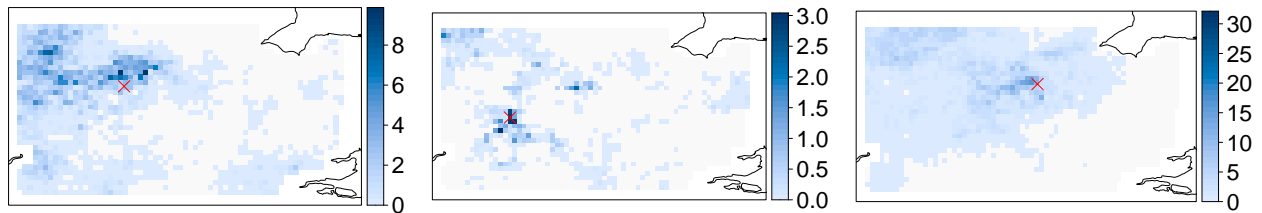


Figure S7: Extreme precipitation fields (mm/hr). Realisations from the fitted models for $Y_{\mathcal{E}}$. The conditioning sites s_0 are given by the red crosses. Scales differ within each panel.

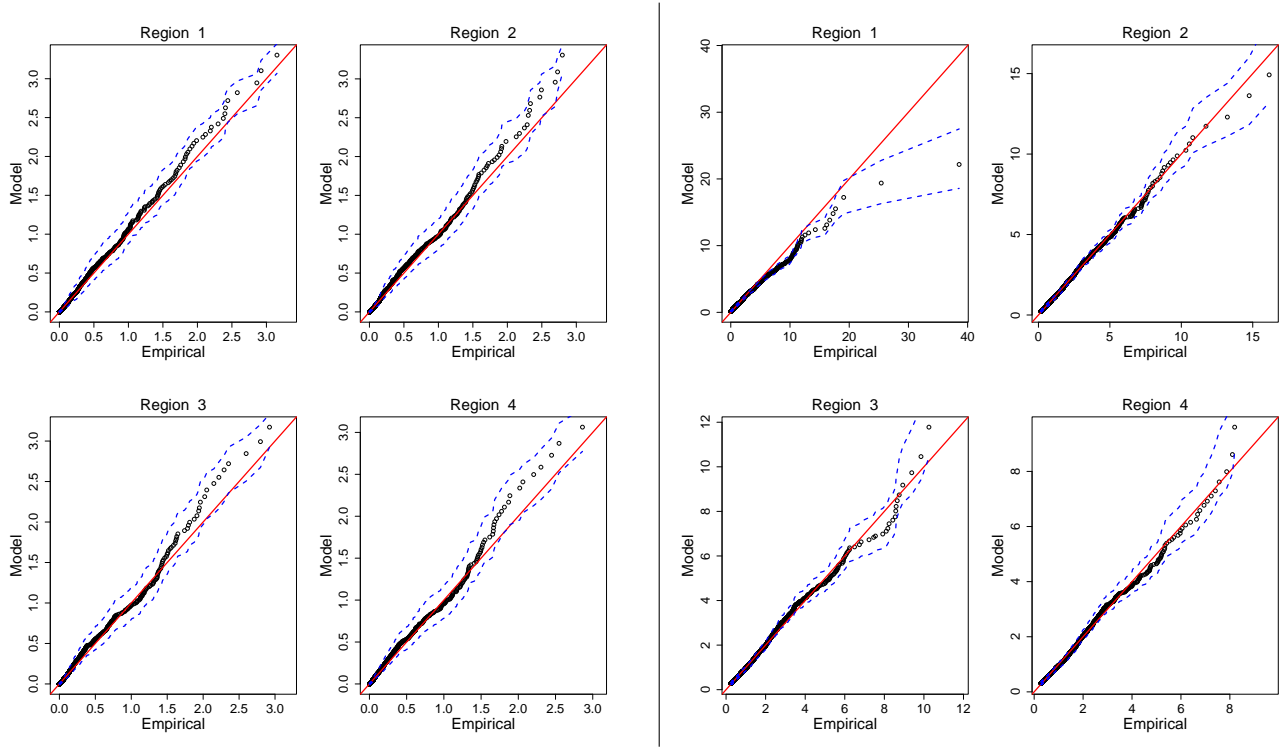


Figure S8: Q-Q plots for the model, and empirical, separate contributions of Y_C and Y_N to $\bar{R}_{M,A}$ for regions of increasing size. Left: $\bar{R}_{N,A}$, right: $\bar{R}_{C,A}$. Probabilities range from 0.8 to a value corresponding to the respective 20 year return level. Blue dashed lines denote point-wise 95% quantile estimates. Regions 1-4 correspond to those illustrated in Figure 1 of the main text.